Mon. Not. R. Astron. Soc. **000**, 000–000 (0000) Printed 3 January 2004 (MN LATEX style file v2.2)

# Dynamical modelling of a remarkable four-armed barred spiral galaxy ESO 566-24

P. Rautiainen[1⋆] H. Salo[1] R. Buta[2]
[1] *Department of Physical Sciences, University of Oulu, P.O. Box 3000, FIN-90014 Oulun yliopisto, Finland*
[2] *Department of Physics and Astronomy, University of Alabama, Box 870324, Tuscaloosa, Alabama 35486, USA*



Received x.x, accepted x.x

**ABSTRACT**
ESO 566-24 is an extraordinary barred galaxy, which has four regularly spaced spiral arms in blue light images. This type of four-armed spiral structure, which is rare among the spiral population, is clearly seen also in near-infrared images, and thus is present in the old stellar population. We have constructed dynamical models of ESO 566-24 in order to understand the cause of its four-armed structure. The disk gravitational potential is determined from near-infrared photometry, and the gas dynamics is modelled as inelastically colliding particles. The resulting morphology and kinematics with different assumed pattern speeds, disk vertical thicknesses and dark halo contributions is compared with observations. Our models can reproduce the main morphological features of this galaxy: the four-armed spiral, and the inner and nuclear rings. The pattern speed of the bar in this galaxy is such that the corotation resonance is well outside the bar radius, $r_{CR}/r_{bar} = 1.6 \pm 0.3$. The four-armed spiral resides in the region between inner and outer 4/1-resonances. Also, the main kinematical features, including bar-induced deviations from circular rotation, are explained by our models. The best fit is obtained when the dark halo contribution is just enough to make the modelled rotation curve match the observed one. This "minimum halo" is rather moderate: luminous matter dominates the rotation curve within the disk region.

**Key words:** galaxies: evolution – galaxies: fundamental parameters – galaxies: kinematics and dynamics – galaxies: spiral – galaxies: structure – galaxies: individual (ESO 566-24)

## 1 INTRODUCTION

Barred galaxies constitute the majority of all spiral galaxies. According to recent near-infrared (NIR) studies, about 70% of disk galaxies have a bar (Eskridge et al. 2000; Knapen et al. 2000). Barred galaxies often have rings or pseudorings in their disks with very distinctive characteristics (Buta & Combes 1996). Depending on its relative size with respect to the bar, a ring can be classified as an outer ring (semi-major axis about twice the bar radius), an inner ring (semi-major axis ≈ bar radius) or a nuclear ring (semi-major axis about 10 % of the bar radius, though the scatter is large) (Buta & Crocker 1993). Although all three types of barred galaxy rings can show enhanced star formation (see, for example, Buta & Purcell 1998), nuclear rings are most prone to starbursts (Maoz et al. 1996; Buta & Combes 2000). In addition to rings, barred spiral galaxies often show offset dust lanes on the leading sides of the bar (assuming trailing spiral arms).

The dynamical behaviour of barred galaxies has been modelled in different ways. Some studies are general, in the sense that no specific barred galaxy is modelled, but they concentrate instead on issues such as the formation and evolution of the bar. In most of these studies, the large-scale bars are suggested to be fast rotators, i.e. their corotation resonance (CR) radius should be near the end of the bar (Sellwood 1981). This is in accordance with gas dynamical simulations of the shapes of the leading offset dust lanes inside the bars (Athanassoula 1992b). Exceptions to fast rotating bars are the studies by Combes & Elmegreen (1993) and Miwa & Noguchi (1998); in the former study a short and slow rotating bar forms in a simulation where the disk was strongly truncated radially, while in the latter, a slow bar forms as a result of an interaction. The contribution of a dark halo inside the radius of the optical disk can have a strong effect on disk dynamics. According to Ostriker & Peebles (1973) a massive halo can inhibit the bar formation, and Debattista & Sellwood (1998, 2000) have shown simulations where the interaction between a bar and a halo decelerates strongly the bar rotation. However, conflicting results have

⋆ E-mail: pertti.rautiainen@oulu.fi

also been published: Athanassoula & Misiriotis (2002) and Athanassoula (2002) show examples where the halo actually promotes bar formation, and Valenzuela & Klypin (2002) found a rather low angular momentum transfer rate from the bar to the dark halo.

In principle, the pattern speed of a bar can be determined from observations for a disk with a well-defined pattern speed (Tremaine & Weinberg 1984). The Tremaine-Weinberg method further assumes that the used tracer component follows the continuity equation, i.e. its intensity is proportional to total density. When these conditions are fulfilled, the pattern speed can be determined from the observed intensity and the line-of-sight velocity along a strip parallel to galaxy major axis. In most of the cases, where this method has been applied, the corotation resonance seems to be near the end of the bar (Kent 1987; Merrifield & Kuijken 1995; Aguerri et al. 2003). Note, however, that due to its limitations, this method has been successfully applied mostly to SB0-galaxies.

Another kinematical method to determine the pattern speed was presented by Canzian (1993) and is based on observed residuals in the velocity field after subtracting the axisymmetric velocity component. In the case of a two-armed spiral, the velocity residuals exhibit an $m = 1$ spiral shape inside corotation, whereas outside corotation, an $m = 3$ spiral should appear. This method was used to determine the pattern speed in NGC 4321 by Sempere et al. (1995) and Canzian & Allen (1997), who found a rather low value, setting the corotation radius about 1.6 – 1.8 times the bar radius. However, the method is very sensitive to noise, and the construction of the axisymmetric velocity component is not trivial. Purcell (1998), who studied a larger galaxy sample, found that only in 7 of 27 Sbc galaxies could the expected pattern be seen in velocity field residuals.

There are several suggested resonance indicators related to morphological details of spiral structure (Elmegreen et al. 1989). Even if these are valid, their application to barred galaxies is not necessarily straightforward: there can be more than one mode in the system. For example the outer spiral arms can have a lower pattern speed than the bar (Sellwood & Sparke 1988). In such cases the pattern speed derived e.g. from the dust lane morphology of the outer arms would not correspond to that of the bar.

The formation of rings in barred galaxies has been explained by the response of the dissipative gas component to the gravitational torque of the bar (Schwarz 1981; Combes & Gerin 1985; Byrd et al. 1994; Buta & Combes 1996; Rautiainen & Salo 2000). The shapes of the rings resemble the shapes of certain closed periodic orbits in barred potentials (Contopoulos & Grosbøl 1989). When the non-axisymmetric perturbation is weak, these rings form very close to resonance radii. The usual resonance identifications are such that the outer rings are located near the outer Lindblad resonance (OLR), the inner rings near the inner 4/1-resonance and the nuclear rings near the inner Lindblad resonance (ILR). Thus if the rotation curve of the galaxy is known, the sizes of the rings can be used to estimate the bar pattern speed. However, these pattern speed estimates can be misleading when the bar perturbation is strong, and the resonance distances based on the linear approximation fail. This is especially the case with nuclear rings, which are located in a region where the relative non-axisymmetric forcing is strong. Furthermore, both nuclear and outer rings can often be affected by another mode in addition to the main bar; nuclear rings by a secondary bar, and outer rings by an outer spiral mode (Rautiainen & Salo 2000; Rautiainen et al. 2002).

The effect of the strength of the bar is taken into account when detailed models for individual galaxies are being constructed. The adopted approach has varied from fitting an analytical mass model to observations (Duval & Athanassoula 1983) to determining the mass model from near-infrared observations (Lindblad et al. 1996; Lindblad & Kristen 1996). In some models, the non-axisymmetric forcing of the bar was not enough to reproduce the spiral structure with the observed extent, and so an unseen oval-shaped component was added (England 1989; Ball 1992). A spiral potential corresponding to the NIR-morphology solved this problem more elegantly (Lindblad et al. 1996). The number of successfully modelled barred galaxies is still quite small, and it is not clear how well the ranges of parameters such as the bar pattern speed and the relative strength of the non-axisymmetric perturbation are known.

We started our modelling project of ringed galaxies with the normal, but rather weakly barred galaxy IC 4214. From the observations (Buta et al. 1999), we constructed a mass model with a few free parameters (Salo et al. 1999). In our best-fitting models both the morphology and kinematics were well reproduced. Following the successful modelling of IC 4214, we extend our studies here by constructing a dynamical model for an extraordinary barred spiral: the four-armed galaxy ESO 566-24.

## 2 A REMARKABLE FOUR-ARMED BARRED SPIRAL

ESO 566-24 is a barred spiral galaxy of de Vaucouleurs revised Hubble type SB(r)b. It was first recognized as being an exceptional example of a four-armed ringed barred spiral galaxy during early stages in the production of the Catalog of Southern Ringed Galaxies (CSRG, Buta 1995). High quality optical CCD images in the $U$, $B$, and $I$ passbands, obtained in follow-up work by Buta & Crocker (1991), reveal an extremely regular four-armed pattern of normal spiral arms, as well as star formation in the inner ring and in a very small previously unknown nuclear ring. These images also revealed a faint, partial outer ring-like pattern that envelopes the four-armed spiral pattern (Buta et al. 1998). Although rings are not rare in barred galaxies, regular four-armed outer spirals are very rare and, if seen at all, appear in a partial manner, as the secondary spiral arcs and two main outer arms seen in NGC 1433 (Buta 1986; Buta et al. 2001).

Buta et al. (1998) showed that the four-armed structure of ESO 566-24 is clearly seen in a NIR $H$-band image. Thus, the pattern is also present in the old stellar population. A recent study of about 200 galaxies in different wavebands by Eskridge et al. (2002) demonstrated that the NIR morphology of galaxies is usually not as dramatically different from the optical morphology as is sometimes stated (Block & Puerari 1999), with multiple-arm and flocculent morphology also being seen in the $H$-band. However, in most

of the cases, two arms dominate, and the extra arms are weaker and usually form as a bifurcation of the main arms. This is not the case with ESO 566-24: the four arms are of about same strength and length.

In this paper, we use numerical models to find the parameter range (pattern speed, mass-to-light ratio) which can reproduce the regular four-armed morphology of ESO 566-24. We study how resonances are located with respect to the observed structures such as rings, and we also identify orbits supporting these structures. Finally, we compare the spectacular morphology of ESO 566-24 with more partial patterns seen in other barred galaxies.

## 3 METHODS

The method used by Salo et al. (1999) in modelling the early-type, weakly-barred spiral galaxy IC 4214 is used here for modelling ESO 566−24. The gas morphology is modelled by inelastically colliding test particles, which move in a rigidly-rotating gravitational potential. We estimate the mass distribution from NIR $H$-band photometry, assuming a constant mass-to-light ratio throughout the disk. Before deprojecting the galaxy image, a bulge–disk decomposition is done, and the resulting bulge component is subtracted from the image. Then the disk surface brightness (and surface density) distribution is approximated using a Fourier decomposition

$$\begin{aligned}\Sigma(r,\theta) &= \Sigma_0(r)\left\{1+\sum_{m=1}^{\infty}A_{\rm m}(r)\cos\left[m\left(\theta-\theta_{\rm m}\right)\right]\right\}\\ &= \Sigma_0(r)+\sum_{m=1}^{\infty}\Sigma_m(r,\theta),\end{aligned} \quad (1)$$

where $r$ and $\theta$ are the polar coordinates, $\Sigma(r,\theta)$ the disk surface density, $\Sigma_0$ the axisymmetric surface density, and $A_{\rm m}(r)$ and $\theta_{\rm m}(r)$ are the Fourier amplitude and phase angles. For our analysis, we used even components $m = 0$ – 8. This introduces smoothing of small scale structure such as star forming regions but has little or no impact on the basic background stellar potential. A similar procedure was adopted by Kranz et al. (2001). From the density components $\Sigma_m$, we then calculate the potential components $\Phi_m$

$$\Phi_m(r,\theta,z=0) = -G\int_0^{\infty}r'dr'\int_0^{2\pi}\Sigma_m(r',\theta')g(\Delta r)d\theta', \quad (2)$$

where $(\Delta r)^2 = r'^2 + r^2 - 2rr'cos(\theta'-\theta)$ and the convolution function

$$g(\Delta r) = \int_{-\infty}^{\infty}\varrho_z(z)((\Delta r)^2+z^2)^{-1/2}dz \quad (3)$$

is used for calculating the effect of the vertical density profile $\varrho(z)$ (normalized to unity when integrated over the vertical direction). In Salo et al. (1999) the gravity softening was used as a measure of finite disk thickness. In this study we use an exponential vertical distribution,

$$\varrho(z) = \frac{1}{2h_z}exp(-|z|/h_z) \quad (4)$$

which has a similar effect. A more detailed description of the potential calculation can be found in Laurikainen & Salo (2002). We have tried scale heights in the range 1/12 – 1/2 times the radial exponential scale length $h_r$ of the disk, corresponding to the change from a very thin disk to an unrealistically thick one; for the morphological type of ESO 566-24, $h_z/h_r \approx 1/6$ is expected (de Grijs et al. 1997; de Grijs 1998). Some tests were made with variable scale height, making the disk thicker in the bar region.

The non-axisymmetric perturbation of the potential is turned on gradually during four bar rotation periods. This procedure was adopted to smoothly "guide" particles to realistic orbits, thus trying to minimize the effect of transient phenomena related to abrupt changes in the potential, e.g. such as a large number of gas particles ending up on crossing orbits.

The gas component is modelled as a two-dimensional disk consisting of 20,000 inelastically colliding test particles. In each collision, the relative velocity component parallel with the line joining the particle centres is reversed and multiplied by the coefficient of restitution. In each time step, only one collision per particle is allowed. The particle motion is integrated using leap-frog integration. The time-step is chosen so that at the radius of the smallest morphological detail, the nuclear ring, one circular rotation period is about 50 steps. In addition to gas particles, we have also made simulations with 200,000 non-colliding "stellar" particles with different initial velocity dispersions. For more details on the simulation code, see Salo et al. (1999).

We use a modified version of the bulge model presented in Buta et al. (1998). We take the average radial profile of the bulge, assume the bulge to be axisymmetric and calculate its gravitational potential using the algorithm described in Kent (1986). As a possible halo component we use an isothermal sphere with a constant core radius, which has a rotation curve

$$v_h(r) = v_\infty\sqrt{\frac{r^2}{r^2+r_c^2}}, \quad (5)$$

where $v_\infty$ is the asymptotic velocity at infinity and $r_c$ is the core radius.

## 4 OBSERVED CHARACTERISTICS OF ESO 566-24

Because the observations and data reduction are described in Buta et al. (1998), we here just give the main morphological and kinematical characteristics of ESO 566-24, concentrating on details which are useful for comparing simulations with observations.

ESO 566-24 has a clear bar component in both visual and NIR-images. The bar is considerably stronger than in IC 4214. It is difficult to judge what would be the best method to determine the bar length. Applying several methods to $H$-band images: e.g., axis ratios of isophotes and local amplitude minima of $m = 2$ and $m = 4$ Fourier components of disk surface brightness, we estimate the bar radius to be $r_{bar} = 18'' \pm 2''$, or about 1.6 times the exponential scale length of the disk, $h_r \approx 11\farcs3$. This is in reasonable agreement with the value adopted in Buta et al. (1998), $r_{bar} = 16\farcs7$. Athanassoula & Misiriotis (2002) use seven different methods to determine the bar length in N-body

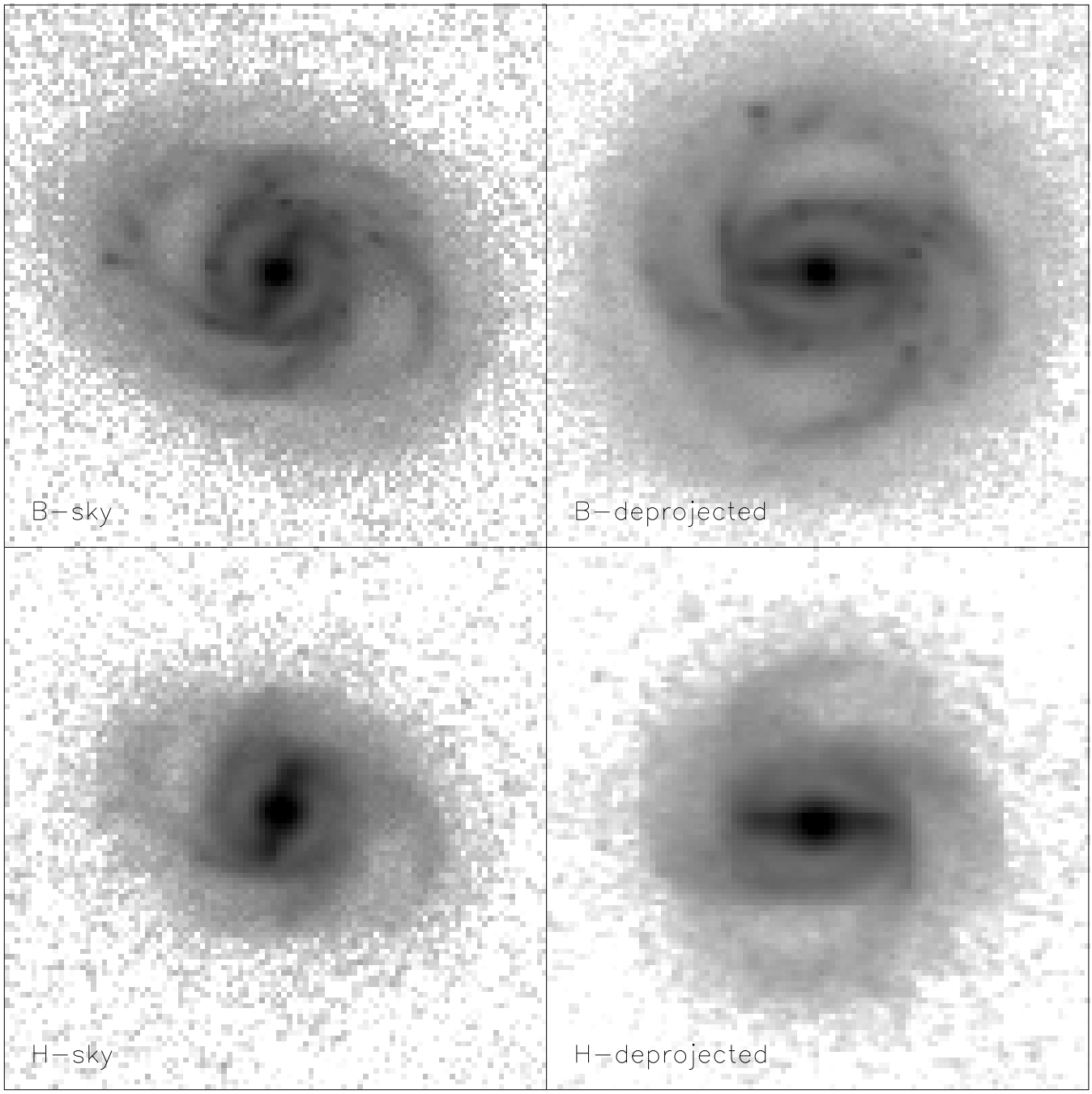


**Figure 1.** B- and H-band images of ESO 566-24. The images on the left side show the galaxy as it is oriented on the sky (foreground stars have been removed) and the images on the right side have been first deprojected and then rotated so that the bar is horizontal. The width of the frames is $120''$.

simulations. However, we found that the complicated morphology of ESO 566-24 made many of these unsuitable (e.g. their $m = 2$ phase angle criterion would give the bar radius in the middle of the spiral pattern). Colour index maps, e.g. $B - I$, show that there are dust lanes on the leading sides of the bar (Buta & Crocker 1991).

The bar is surrounded by an inner ring, which appears circular in the plane of the sky but deprojects to an ellipse parallel with the bar major axis for the adopted orientation parameters: position angle $PA = 73^\circ$ and inclination $i = 43^\circ$ (Buta et al. 1998). Parallel alignment is a normal characteristic of barred galaxy inner rings (Buta 1995). The deprojected semimajor axis radius of the inner ring is about $19''$. There is also a nuclear ring with a semimajor axis radius of about $4''$. The four bright spiral arms extend between $20''$ and $40''$. The arms start from the inner ring, two from its major axis and the other two from the minor axis. Both the inner ring and the four spiral arms can be seen also in the NIR $H$-band image. There is also a single outer spiral arm or a partial outer ring, that is not connected to the

**Table 1.** The main parameters for the three model families D, M and H. The H-band mass-luminosity ratios of the bulge $(M/L)_{\rm B}$ and the disk $(M/L)_{\rm D}$ are given in solar units, assuming $M_{H\odot} = 3.37$ and the distance being 45 Mpc. Also listed are the parameters determining the halo rotation curve: velocity in infinity $v_\infty$ in kms$^{-1}$ and core radius $r_c$ in arcseconds.

| Model family | $(M/L)_{\rm B}$ | $(M/L)_{\rm D}$ | $v_\infty$ | $r_c$ |
|---|---|---|---|---|
| D | 1.3 | 1.3 | | |
| M | 1.2 | 1.2 | 152 | 40.0 |
| H | 1.2 | 0.54 | 180 | 20.0 |

four-armed spiral (Buta et al. 1998). Fig. 1 shows *B*- and *H*-band images (as observed in the sky and deprojected) of ESO 566-24.

The rotation curve inferred from the velocity field (see Fig. 2) shows signs of probable non-circular motions: in the inner parts it rises steeply, then it has a short flat part at about 120 km s$^{-1}$. Outside this area, it rises steeply again to the peak value, after which it quickly drops to the constant level of about 190 km s$^{-1}$. It is probable that the peculiar inner rotation curve is at least partly caused by non-circular motions induced by the bar, since axisymmetric rotation curves constructed from any realistic combinations of bulge, disk and halo cannot produce such a structure. Also the zero velocity curve of the velocity field implies the presence of non-circular motion. However, the effect is not as strong as in IC 4214 because in ESO 566−24, the orientation of the bar is almost perpendicular to the line of nodes, and hence little of the radial component of the velocity vector projects to the line of sight (see also Buta 1988).

## 5 MODELLING

We have constructed three major sets of models: series D without a halo component, series M with a moderate halo and series H with a dominating halo (see Table 1). In all of these model series, we have varied several parameters such as the bar pattern speed and the disk thickness.

The left side frames of Fig. 2 compare the rotation curves of models of series D (no halo), M (moderate halo) and H (dominating halo) with a similar disk thickness ($h_z/h_r = 1/6$). Also shown are the circular velocity points determined from the observed velocity field using the method presented by Warner et al. (1973). If we adopt the definition of a maximal disk (or disk+bulge) by Sackett (1997): a disk is maximal if its rotation speed at radius $r_{2.2} = 2.2\ h_r$ (usually close to the peak of the disk rotation curve) is 75–95% of the total circular speed at this radius, then our moderate halo series M resides near the lower limit of maximal disks. Perhaps a better name would be a minimum halo model: only such an amount of halo was included that is needed to make the outer curve as flat as the observed rotation curve.

The right side frames of Fig. 2 show the corresponding "frequency diagrams", i.e. curves showing $\Omega$, $\Omega \pm \kappa/2$ and $\Omega \pm \kappa/4$, where $\Omega$ is the circular frequency and $\kappa$ is the epicyclic frequency. The inner parts of the models have very similar rotation curves, and thus with the same pattern speed, the inner resonance distances (ILRs and inner 4/1) would be about the same. On the other hand, the outer resonance radii are different. For example, the distance between the inner and outer 4/1-resonances is larger in models with a halo than in models without it. Throughout this article we use km s$^{-1}$arcsec$^{-1}$ as a unit of pattern speed. We denote models of each mass model series with the pattern speed: for example model D6.7 is a series D model with pattern speed $\Omega_b = 6.7$ km s$^{-1}$arcsec$^{-1}$. At the adopted distance of 45 Mpc, 1 km s$^{-1}$arcsec$^{-1}$ corresponds to about 4.6 km s$^{-1}$kpc$^{-1}$ and the length of a simulation is about 2.7 Gyr (about 14 bar rotation periods in our best-fitting case).

### 5.1 The effect of model parameters

#### *5.1.1 The effect of disk thickness*

One of the main model parameters is the disk thickness. We have made simulations with a range of the disk scale height from 1/12 to 1/2 of the disk scale length, which should cover the plausible range of values for the disk thickness. In Fig. 3 we show the Fourier components of the tangential force relative to the axisymmetric radial force (total of bulge, disk and halo) as a function of radius for different mass models.

As can be seen in Fig. 3, the $m = 2$ component has one maximum, at about 12″, well inside the bar. The $m = 4$ component has two clear maxima, one coinciding with the $m = 2$ maximum, and the other broader one in about the middle of the four-armed spiral structure. The $m = 6$ and $m = 8$ components have also two maxima, the inner coinciding with the $m = 2$ maximum, and the outer ones being inside the outer $m = 4$ maximum.

As a measure of bar strength, we use the relative tangential force $Q_T$ (Combes & Sanders 1981):

$$Q_T(r) = F_T^{max}(r) / < F_R(r) >, \qquad (6)$$

where $F_T^{max}(r)$ is the maximum of tangential force at a given radius $r$, and $< F_R(r) >$ is the azimuthally averaged radial force at the same radius. The maximum of $Q_T(r)$ over radius, or $Q_b$, has been used as a single measure of bar strength by Buta & Block (2001) and Laurikainen et al. (2002). From Fig. 3 we can see that in our basic mass models, the extreme values of the $Q_b$-parameter vary from 0.1 to 0.47 when going from the thickest disk models of series H to the thinnest disk models of series D. In each mass model series, the models with the thinnest disks have about twice as strong bars as models with thickest disks if measured by $Q_b$. One can also see from Fig. 3 that the effect of disk thickness on $Q_T$ is much weaker in the region of the spiral arms.

In Fig. 4 we show the effect of disk thickness on the simulated gas morphology. When comparing with the observed four-armed spiral of ESO 566-24, we see that in the D-series the fit is best when the disk is very thick ($h_z/h_r = 1/2$). In series M, the best fit is obtained with a thinner disk (both $h_z/h_r = 1/12$ and $h_z/h_r = 1/6$ give a fairly good fit). In series H, the spiral response to the potential is always too weak. This can be explained by the weakness of the non-axisymmetric perturbation at the spiral region: it is less than half of that in series' M and D. We can also see that the size of the nuclear ring depends on the disk thickness: a thicker disk leads to a larger ring due to the reduced non-axisymmetric perturbation at its location, shifting the

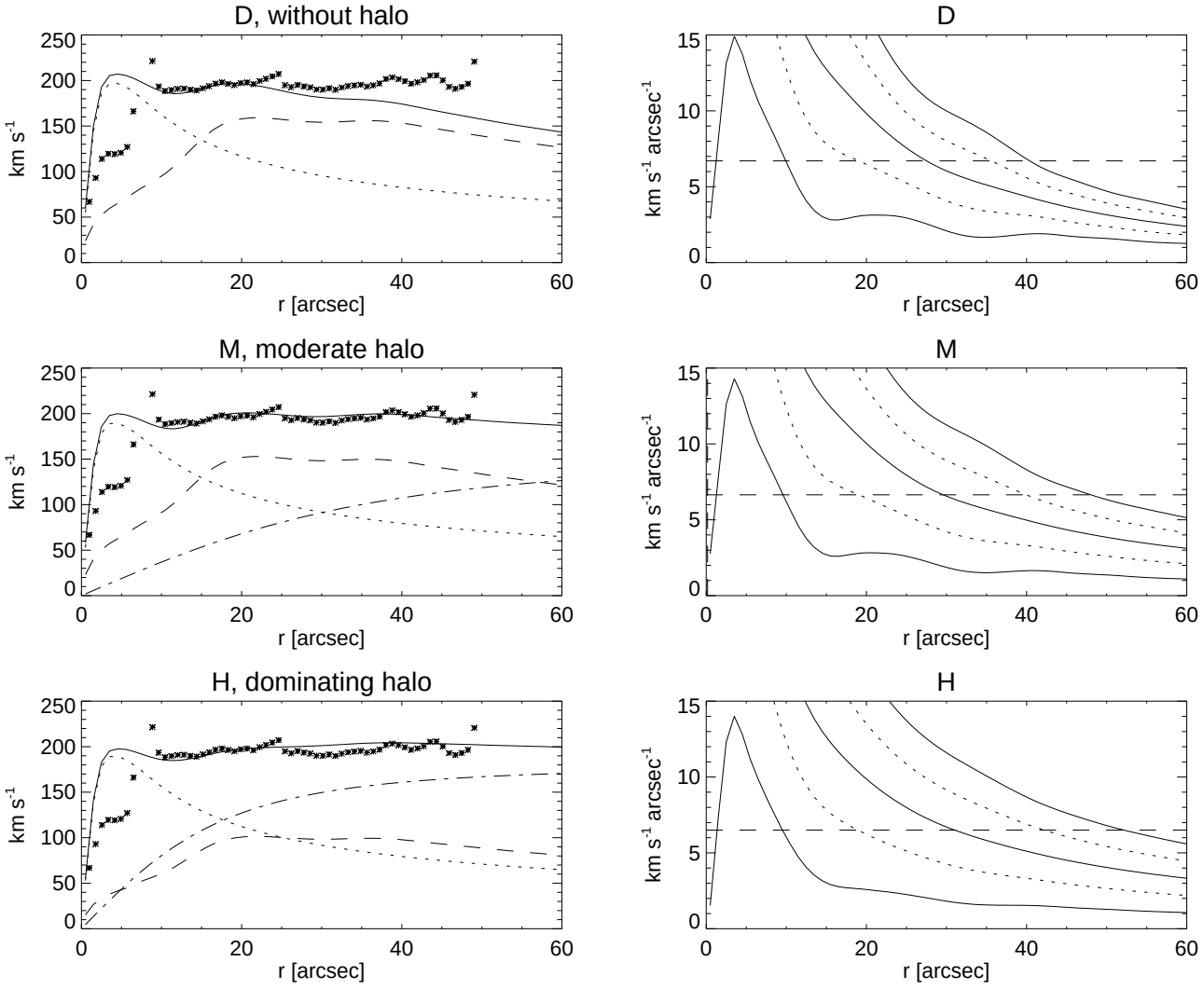


**Figure 2.** Comparison between three models with different mass distributions (see Table 1). The frames on the left side show the rotation curves, total rotation curve indicated as a continuous line, bulge as a dotted line, disk as a dashed line and the halo as a dash-dotted line. The asterisk symbols show circular velocities determined from the observed velocity field (see text). The frames on the right side show $\Omega$ (thick continuous line), $\Omega \pm \kappa/2$ (thin continuous lines) and $\Omega \pm \kappa/4$ (dotted lines) The dashed horizontal line shows the pattern speed at which the semimajor axis of the inner ring ($19''$) coincides with the inner 4/1-resonance. The $M/L$ of the bulge was chosen in each case so that the rotation amplitude at $20''$ corresponds with the observed one.

ring closer to linear ILR. The axial ratio of the inner ring is not very sensitive to $Q_b$, which is not surprising, because the location where the maximum of $Q_T$ is reached is well inside the ring. At the ring region, $Q_T$ varies less than its maximum value $Q_b$ when compared in models with different disk scale heights.

### *5.1.2 The effect of pattern speed*

For each basic mass model, we ran a series of simulations with five different pattern speeds. The middle pattern speed of each series was chosen so that the semimajor axis radius of the inner ring coincides with the inner 4/1-resonance, and the highest pattern speed so that its corotation radius is 1.1 times the bar radius. The other values of the pattern speed were chosen around the middle one with a step size 1.2 km s$^{-1}$arcsec$^{-1}$.

Fig. 5 shows the effect of the pattern speed on gas morphology in series D. When the pattern speed rises, the nuclear ring becomes smaller. With the highest pattern speed, $\Omega_b = 9.5$, the inner ring disappears and the nuclear ring becomes very elongated and parallel with respect to the bar. Four-armed spiral structure can be seen clearly in models D5.5 and D6.7. Both at higher and lower pattern speeds, the spiral tends to become two-armed. Several models in this and other mass model series have weak overdensities of gas particles in the bar area resembling leading offset dust lanes. These features are stronger in the early phases of simulations and more or less disappear during the simulations. These features move closer to the bar when the pattern speed is

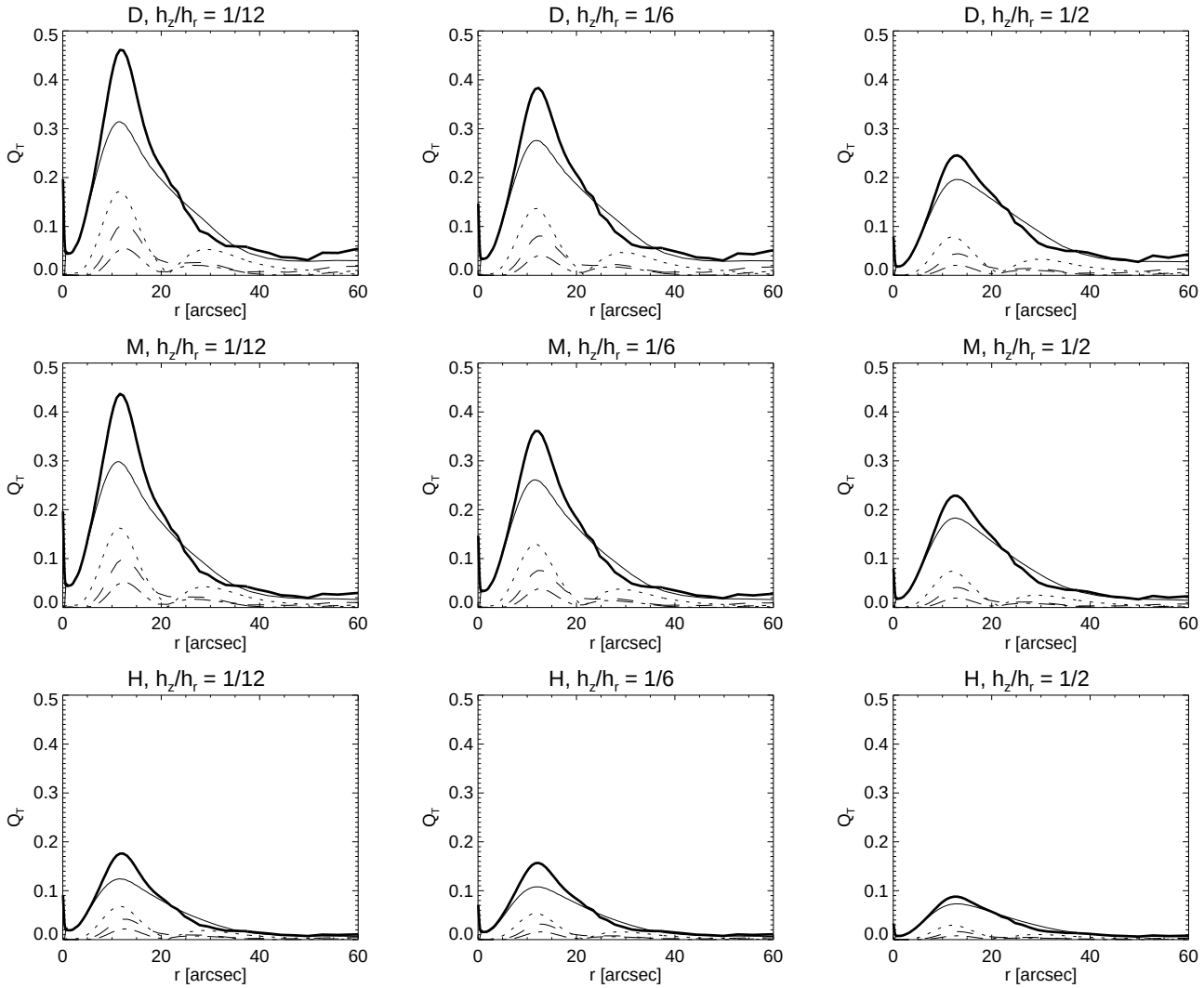


**Figure 3.** The relative tangential force in models without a halo (top row), with a moderate halo (middle row) and with a strong halo (bottom row). The thick continuous line shows the maximum, whereas the m=2 component is indicated with a thin continuous line, m=4 component with a dotted line, m=6 with a dashed line and m=8 with a dot-dashed line. Note that owing to phase differences, the maximum is less than the sum of the amplitudes of the different components.

increased, but in general they are too vague to be reliably compared with the observed dust lanes.

Fig. 6 shows the effect of the pattern speed on the gas morphology in series M, which has a moderate halo component. The basic trend is quite similar as in the models without a halo, but the four-armed spiral appears in a larger pattern speed range (models M5.5 – M7.9), and is also more pronounced, the arms being longer and sharper.

Fig. 7 shows the effect of the pattern speed on gas morphology in series H, with a dominating halo. The non-axisymmetric force is too weak to produce sharp spiral arms, and thus only weak spiral features appear, exhibiting a four-armed structure in models H5.5 – H7.9.

### *5.1.3 Miscellaneous parametric dependencies*

We have also checked the effects of various other model parameters: the number of Fourier components that were used to calculate the gravitational potential, the initial gas distribution, the bar turn-on speed, the collision frequency, and the coefficient of restitution. All these have only a minor effect when compared to disk thickness and the pattern speed of the bar.

The inclusion of Fourier component $m = 4$ and the higher ones makes the four-armed spiral more pronounced. When only $m = 0$ and $m = 2$ components are included, the response is not a clear $m = 4$ spiral, but resembles model M6.7 with a thick disk. The other mass models follow similar trends. We have also made simulations where we include the odd components of the Fourier decomposition. This causes some asymmetry to the models, especially in the region where spiral arms emerge from the inner ring, but the effect is small.

We found that the bar turn-on speed can affect the innermost morphology: when the bar was turned on too abruptly (obtaining full strength in one or less bar rota-

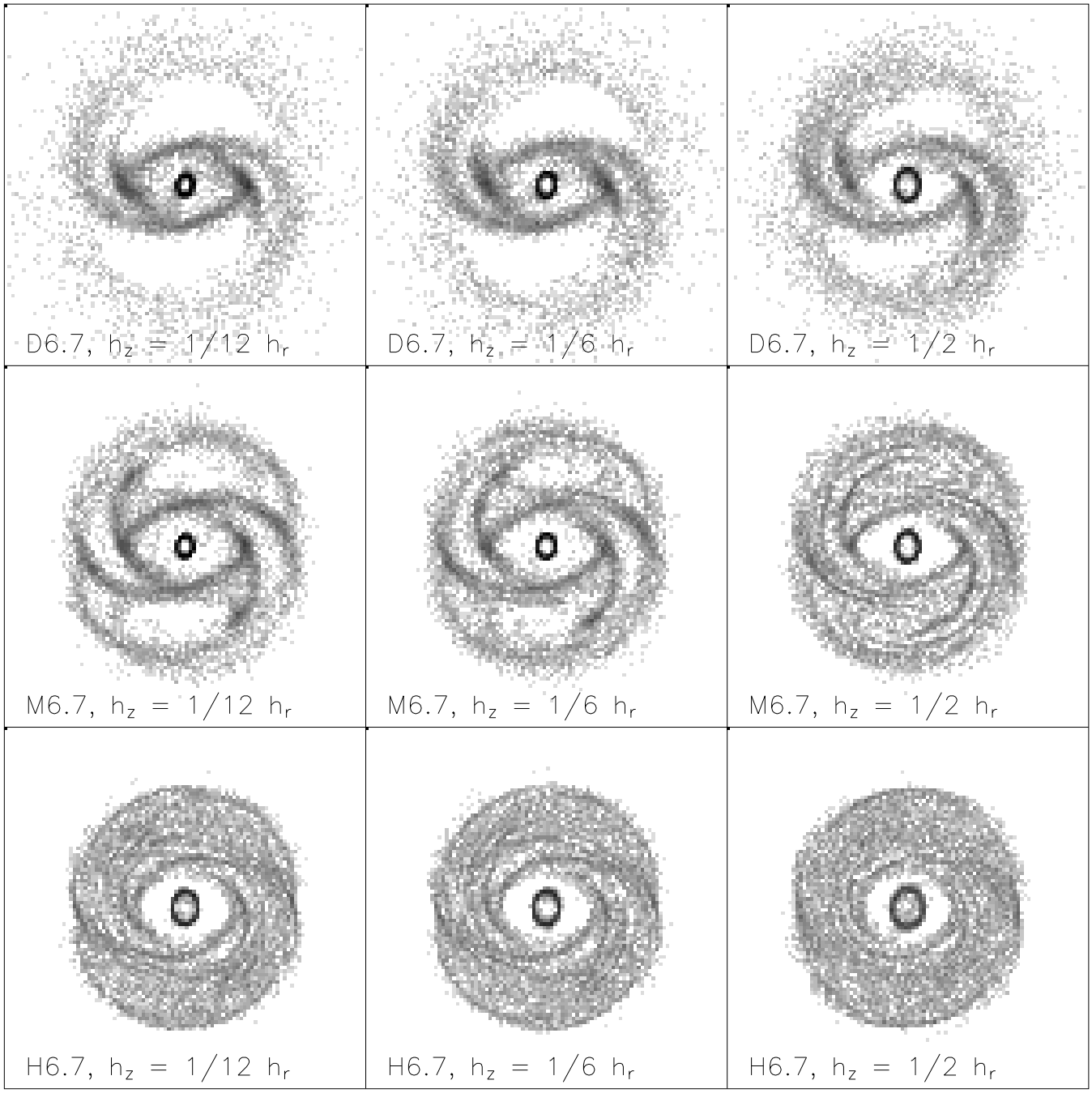


**Figure 4.** The effect of the disk thickness in models from the disk-dominated series D (top row), series M with a moderate halo (middle row) and the halo-dominated series H (bottom row). Compare to Fig. 3 showing the strength of the non-axisymmetric force field in each case. The width of the frames is 120″. The models are shown one bar period after the bar has reached its full strength.

tion periods), some of the nuclear rings collapsed toward the centre or became very elongated and parallel to the bar. This is probably due to the high amount of intersecting orbits. When the bar reached its full strength more gently (in 2–4 bar rotation periods), these gas particles were slowly "guided" to orbits perpendicular with respect to the bar. However, when the pattern speed was high enough, even the gradual bar turn-on time could not save the nuclear rings, and the short-lived rings were destroyed before the bar reached its full strength. The reason for such behaviour is that the number of intersecting orbits increases when $\Omega_b$ is increased. This was confirmed by simulations using non-colliding test particles.

We studied the effect of collision frequency by making selected simulations with different gas particle sizes. If extreme values are ignored, the collision frequency affects mainly the sharpness of features and their formation timescale. However, the main morphological features are not strongly dependent on the collision frequency. We also studied the effect of the coefficient of restitution $\alpha$. Changing $\alpha$

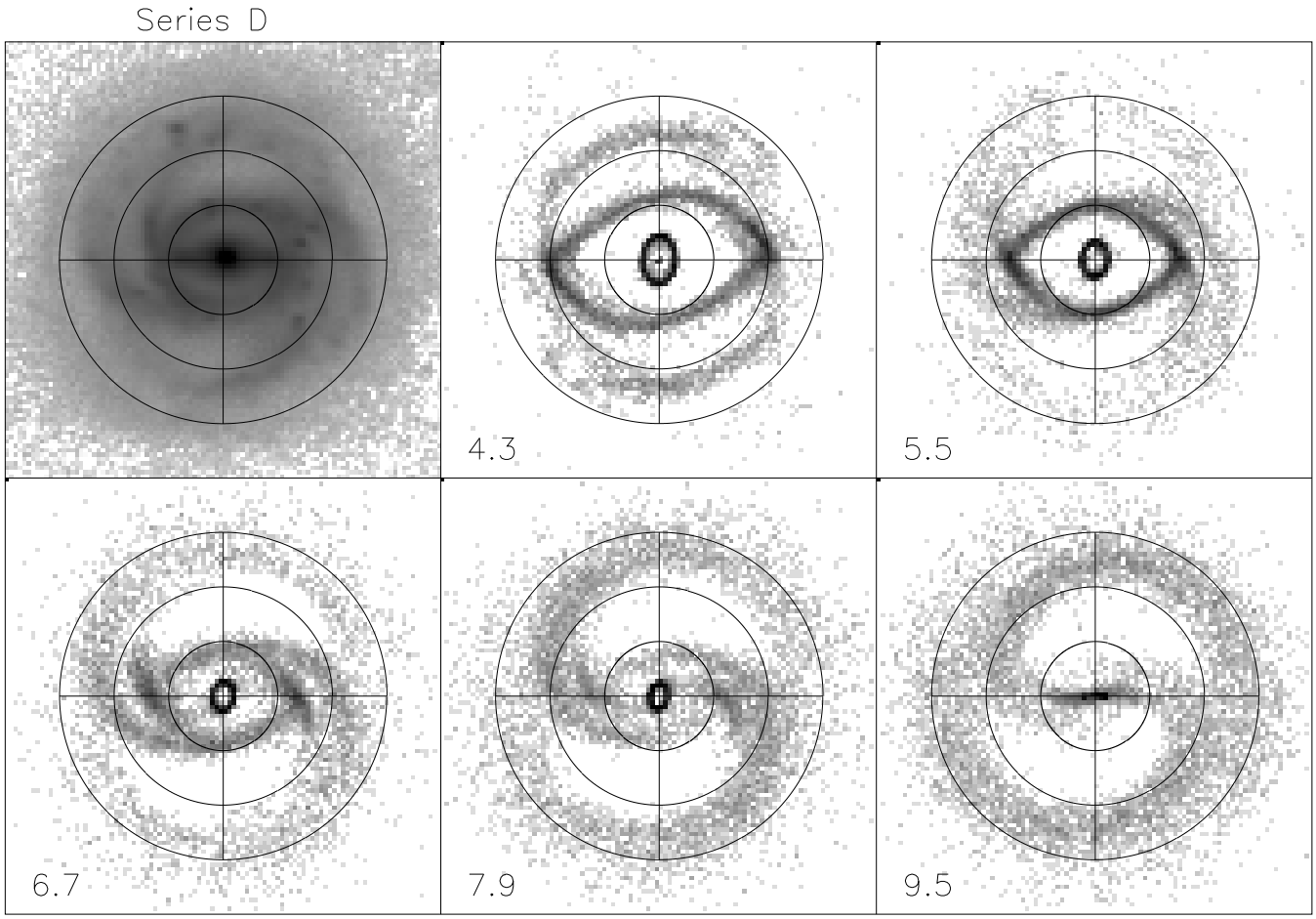


**Figure 5.** Pattern speed series for models without a halo compared with a B-band image of ESO 566-24. The circles indicate radii of 15, 30 and 45″. The width of the frames is 120″. The models are shown one bar period after the bar has reached its full strength.

between our standard value, 0.0, and 0.5 has only a minor effect on the morphology. The greatest difference is in nuclear ring: adopting higher values of $\alpha$ produces a smaller and thicker ring.

### 5.2 A search for the best fit

We use here the results of the previously presented simulation series to deduce the probable range of the essential model parameters.

#### *5.2.1 Morphology*

The top row of Fig. 8 shows the time evolution of morphologically-selected best-fitting models from the D- and M-series (in series H the spiral response is always very weak). The models without a halo, including the one shown, tend to have a problem with the positions of the four spiral arms: the arms are not equally spaced in azimuth. Instead of a clear $m = 4$ spiral, the structure more resembles two pairs of arms, or doubled arms. Another fault is the lack of "morphological longevity" in the models of series D: the spiral structure disperses in just a few bar rotation periods. The models with a moderate halo have more equally spaced and longer lasting spiral structure. A common trend in their long-term evolution is that when the spiral arms weaken owing to gas flow, the minor axis arms become relatively stronger than the major axis arms. This causes some models to become essentially two-armed in their later phases. Both model series produce slightly too pointed and elongated inner rings. Because the overall fit of the spiral morphology is better and due to its longevity, we prefer model M6.7 over model D6.7.

We have tried to improve the pattern speed estimate by making several simulations around model M6.7. Judging by the spiral morphology and the size of the inner ring, we derived $\Omega_b = 6.9 \pm 0.5$ km s$^{-1}$arcsec$^{-1}$, or about $33.7 \pm 2.3$ km s$^{-1}$kpc$^{-1}$. Fig. 9 compares this morphological best-fitting model M6.9 with the $B$-band morphology of ESO 566-24. The resonance radii corresponding the epicycle approximation are indicated as circles. The nuclear ring is between two inner Lindblad resonances (1.3″ and 9.4″) and the inner ring is close to the inner 4/1-resonance (17.9″). The four-armed spiral structure is between the inner and outer 4/1-resonances (38.7″). The OLR radius (46.5″) is outside the spiral structure. When compared with the deprojected image of ESO 566-24, we can see that the bar ends well before the corotation resonance radius (28.5″), near the in-

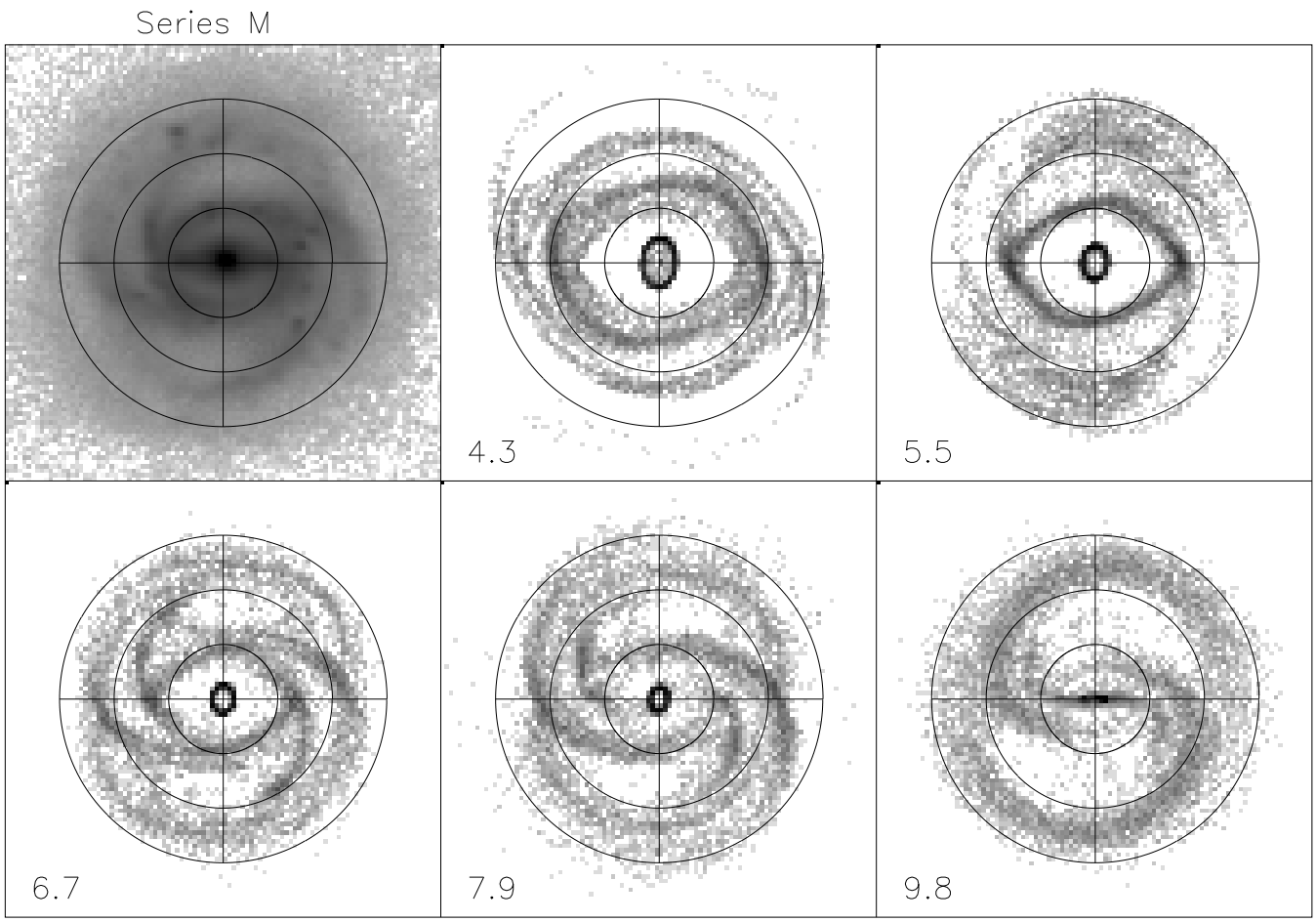


**Figure 6.** Pattern speed series for models with a moderate halo. The circles indicate radii of 15, 30 and 45″. The width of the frames is 120″. The models are shown one bar period after the bar has reached its full strength.

ner 4/1-resonance. Using the bar radius $18'' \pm 2''$, this gives $r_{CR}/r_{bar} = 1.58$. Combining the uncertainties in the determination of $r_{bar}$ and $\Omega_b$, we finally get $r_{CR}/r_{bar} = 1.6 \pm 0.3$.

The morphology of two "stellar" populations consisting of non-colliding test particles is also shown in Fig. 9. Both the low and medium velocity dispersion components (neither of these components should be expected to represent the self-gravitating stellar populations but more as a tracer of dynamics) have a strong contribution of orbits resembling the closed $x_2$-orbits (aligned perpendicular with respect to the bar) of analytical bar potentials (Contopoulos & Grosbøl 1989). Here, we call these orbits $x_2$-like orbits instead of $x_2$-orbits for two reasons. First, they are orbits of individual particles in our simulations, not exactly closed orbits found by iteration. Second, our potential differs from analytical bar potentials, because it is calculated from NIR-photometry. Thus, our bar is not straight (this causes the orientation of the inner orbits to be tilted with respect to the outer parts of the bar) and the contribution of the spiral arms is also included. Of course, the situation is somewhat similar in real galaxies, which do not accommodate idealistic bars. In addition to $x_2$-like orbits, the presence of $x_1$-like orbits (aligned parallel with respect to the bar) can be seen in both populations. It is evident that there is no support for a strong bar structure outside the inner 4/1-resonance. In the medium dispersion case, there is a low density feature with a minor-to-major axis ratio of about 0.5, that is aligned with the bar and reaches almost to corotation. However, it is more like an oval or a lens than a bar.

In Fig. 10 we compare the nuclear morphology of low dispersion collisionless populations in two different bar pattern speeds with the corresponding gas morphology and we also show some selected orbits of individual stellar particles. In model M6.9, there is a "stellar" nuclear ring, which almost reaches the outer ILR radius of the epicycle approximation. The gaseous nuclear ring is considerably smaller. A possible reason for this difference is the crossing orbits, where colliding particles cannot stay. The outer $x_2$-like orbits are crossing both a considerable population of $x_1$-like orbits and other $x_2$-like orbits. Furthermore, the outermost orbits do not form (almost) closing loops, although they retain a perpendicular orientation with respect to the bar. The region suitable for non-crossing $x_2$-like orbits corresponds quite well with the size of the gaseous nuclear ring. In model M9.8 with higher pattern speed, the $x_2$-like orbits do not reach as close to the linear outer ILR radius. Their domain is also much narrower, which could explain why the gaseous nuclear ring has the orientation of $x_1$-like orbits.

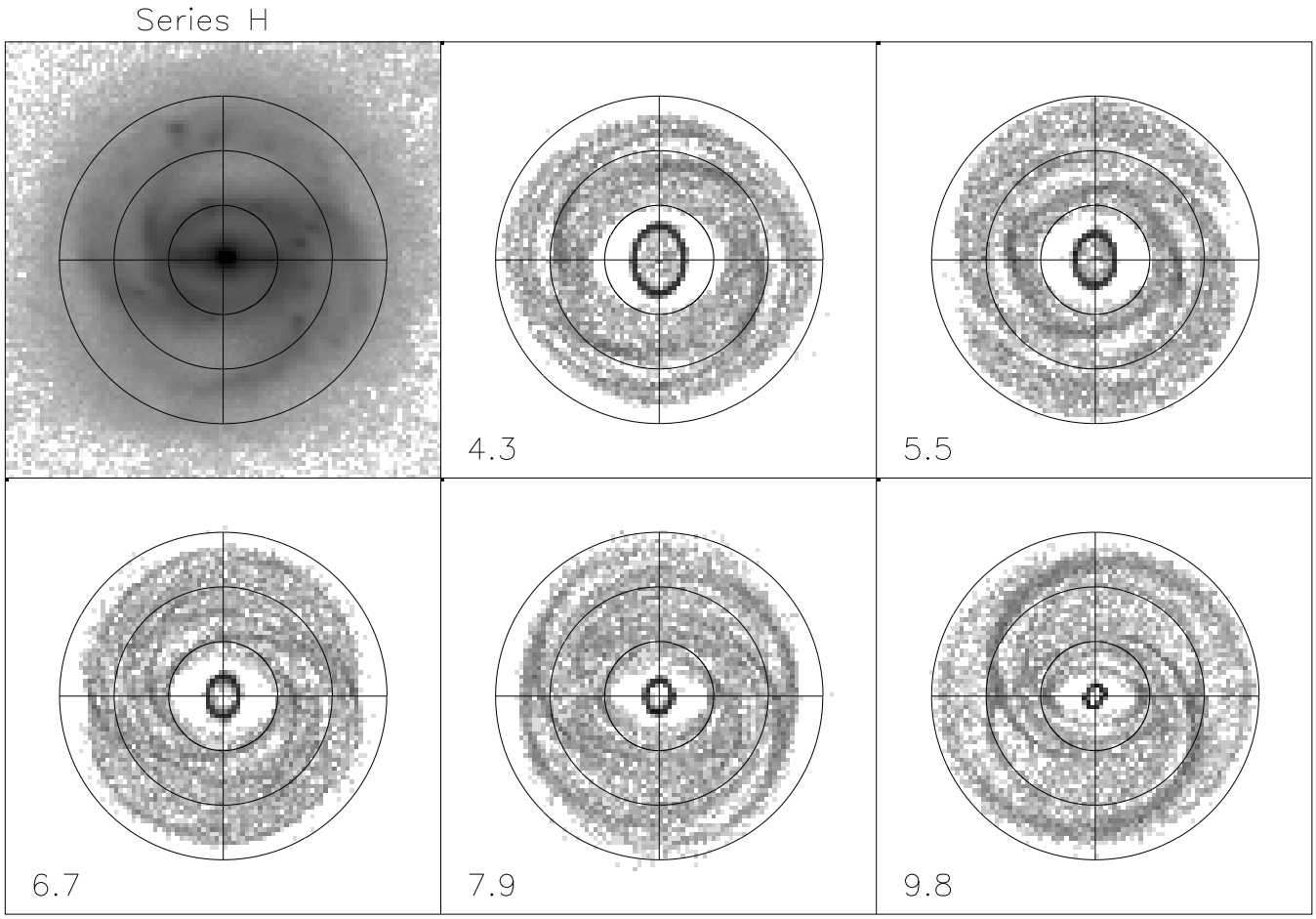


**Figure 7.** Pattern speed series for models with a strong halo. The circles indicate radii of 15, 30 and 45″. The width of the frames is 120″. The models are shown one bar period after the bar has reached its full strength.

We followed particle orbits in the region of the four-armed spiral and found a large number of particles librating around Lagrangian points $L_4$ and $L_5$ (Binney & Tremaine 1987), which are close to the bar minor axis. However, the spiral structure cannot be explained by any single orbit type.

Fig. 11 shows the azimuthal variations of relative surface density at different radii both in observations and in our best-fitting model. We can see that although the $m = 2$ component is dominating near the bar end, there are soon signs of an $m = 4$ pattern. In the midst of the spiral structure, at about 35″, all four arms are of about equal strength in the $H$-band image, and the arm-interarm density contrast can be locally almost as high as 2.0 (about 0.7 magnitudes). Such high values in NIR-images have been found in only a few galaxies, such as M 51 (Rix & Rieke 1993). Comparison between the gas component of model M6.9 and the $B$-band morphology of ESO 566-24 shows that the locations of intensity maxima are quite well fitted in the spiral arms. In the stellar component, the match is worse, which is not surprising since the model is not self-consistent.

### *5.2.2 Kinematics*

In our previous modelling object, IC 4214, the fine details of the zero velocity contour of the velocity field were valuable in determining the bar strength and other model parameters. Even though the non-axisymmetric perturbation in ESO 566-24 is considerably stronger than in IC 4214, the zero velocity contour is rather featureless. This is due to the unfavourable orientation of the bar with respect to the line of nodes.

On the other hand, the "rotation curves" constructed using the method introduced by Warner et al. (1973) shows the effect of non-circular velocities. The clearest features affected by the non-axisymmetric perturbation are located inside 10″, just inside the peak of $Q_T$, the relative non-axisymmetric force. Furthermore, the flatness of the outer rotation curve clearly indicates that at least some amount of halo is needed (supposing constant M/L-ratio).

Fig. 12 shows comparison of selected rotation curves constructed from the modelled velocity field (data from 10 time steps are summed) with the observed one. The observed velocity field does not have velocity information from the whole disk area, for example, the four-armed spiral structure is incompletely covered. On the other hand, many of

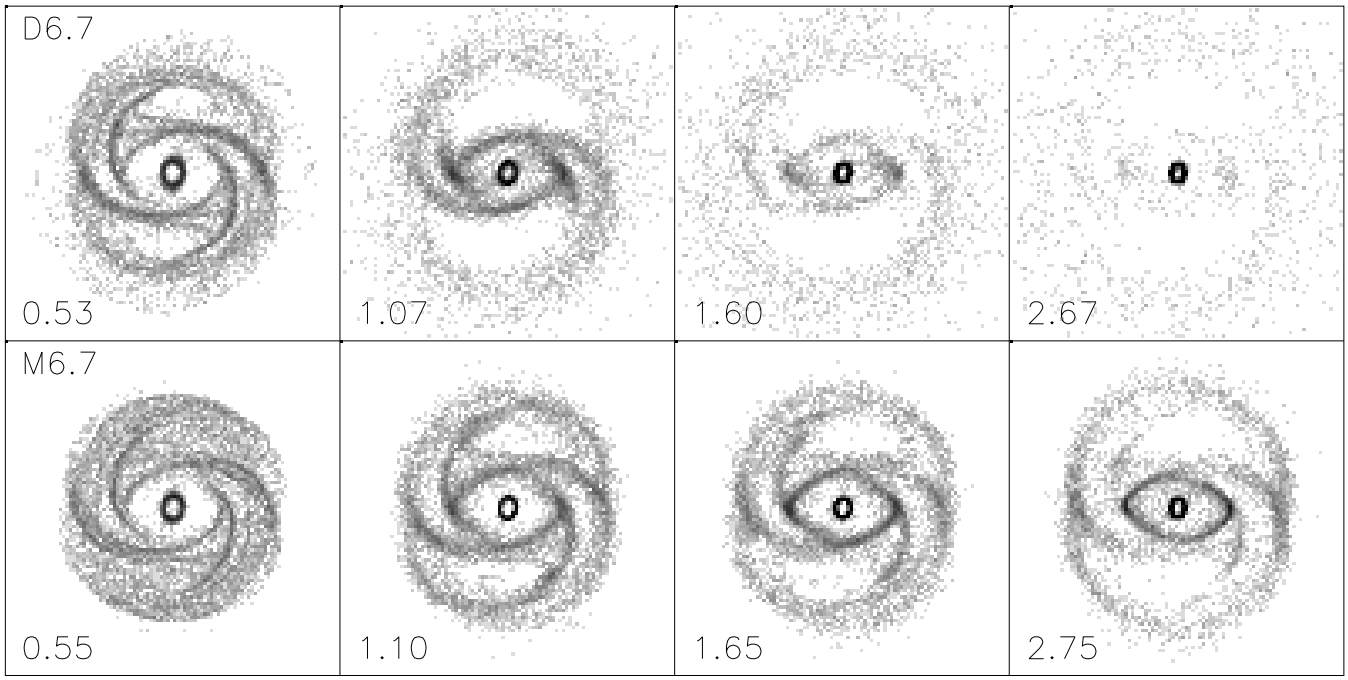


**Figure 8.** The time evolution of two models from series D and M. The width of the frames is 120″ and time is shown in simulation Gyr. The timesteps of the models are the same, but the times differ due to different mass scaling.

our models include gas particles practically in the whole disk area. This is potentially dangerous when it comes to comparing the observed and modelled kinematics. To diminish this problem we adopted a density threshold to the modelled velocity field. In some cases, this can have a notable effect on the inner part of the modelled rotation curve.

Our morphologically fitted "standard" model, M6.9 (frame a), gives a rather good fit with the position of the velocity jump near 10″. The inner parts show also a similar trend as the observed kinematics. However, the rotation amplitudes do not fit as well. Whereas the outer rotation amplitude is well fitted, the modelled velocity is too high inside 25″. A model with a thicker disk (frame b) gives a better fit, but the rotation amplitude inside 6″ is still too high, by about 40 km $s^{-1}$. This problem cannot be solved by changing the disk thickness or the pattern speed. A considerable increase of pattern speed destroys the two-stage structure of the rising part of the rotation curve, as is highlighted by the kinematics of the model M9.8 (frame c).

To get better kinematical fit, we tried changing the relative masses of bulge, disk and halo (the radial profiles were not modified). In model B6.3 (frame d), where $(M/L)_{\rm B} = 0.86$, $(M/L)_{\rm D} = 1.02$ and $v_\infty = 219$ km $s^{-1}$ we could get the difference between the inner velocities as low as $10-20$ km $s^{-1}$. With the pattern speed 6.3 km $s^{-1}$arcsec$^{-1}$, which sets the inner 4/1-resonance to approximately same distance as in model M6.9, the inner and nuclear rings have about the same size as in model M6.9. However, the four-armed spiral is not well fitted: instead of long spiral arms, we get several threaded arms. This is due to the increased halo contribution. If we further decrease the relative contribution of the bulge in order to reach the observed rotation amplitude, the nuclear ring changes its shape and orientation, by becoming dominated by $x_1$-like orbits. Its morphology is then rather similar to the nuclear ring in model M9.8, and the central kinematics shows a peak instead of a drop. Thus, combining the morphological and kinematical comparison, model M6.9 is our best-fitting solution for ESO 566-24.

The behaviour of the determined rotation curve inside 10″ is related to two factors: the orientation of the bar, i.e. its major axis is close to the kinematical minor axis, and to the orientation of $x_1$- and $x_2$-like orbits with respect to the bar. In the case of pure elliptical orbits with major or minor axis parallel with the kinematical major axis, the resulting rotation curve is either below (orbit's major axis parallel with the kinematical major axis) or above (orbit's minor axis parallel with the kinematical major axis) the local circular velocity (Teuben 2002). In barred galaxies, the shapes of orbits deviate from pure ellipses, but this approximation is still helpful to understand the general trends in the kinematics of ESO 566-24. Now, the low velocities in the region inside 6″ are caused by $x_2$-like orbits, whose major axis is perpendicular with respect to the bar major axis. The velocity of these orbits near the bar minor axis (the major axis of the orbits), is much lower than the local circular velocity of the azimuthally averaged rotation curve. This is also close to the kinematical major axis, and thus the determined rotation curve in this region is below the axisymmetric rotation curve calculated from the mass distribution.

Similarly, the velocity peak near 10″ is caused by $x_1$-like orbits, which are parallel to the bar. In this distance, they are near their minor axis, and the velocity is higher than the local circular velocity. The location of this feature depends on the extent of $x_2$-like gas particle orbits. This is in part dependent on the pattern speed and the amplitude of the nonaxisymmetric perturbation. Also evolutionary effects are present: the jump can move inwards when the size of the nuclear ring decreases. In some simulations the jump

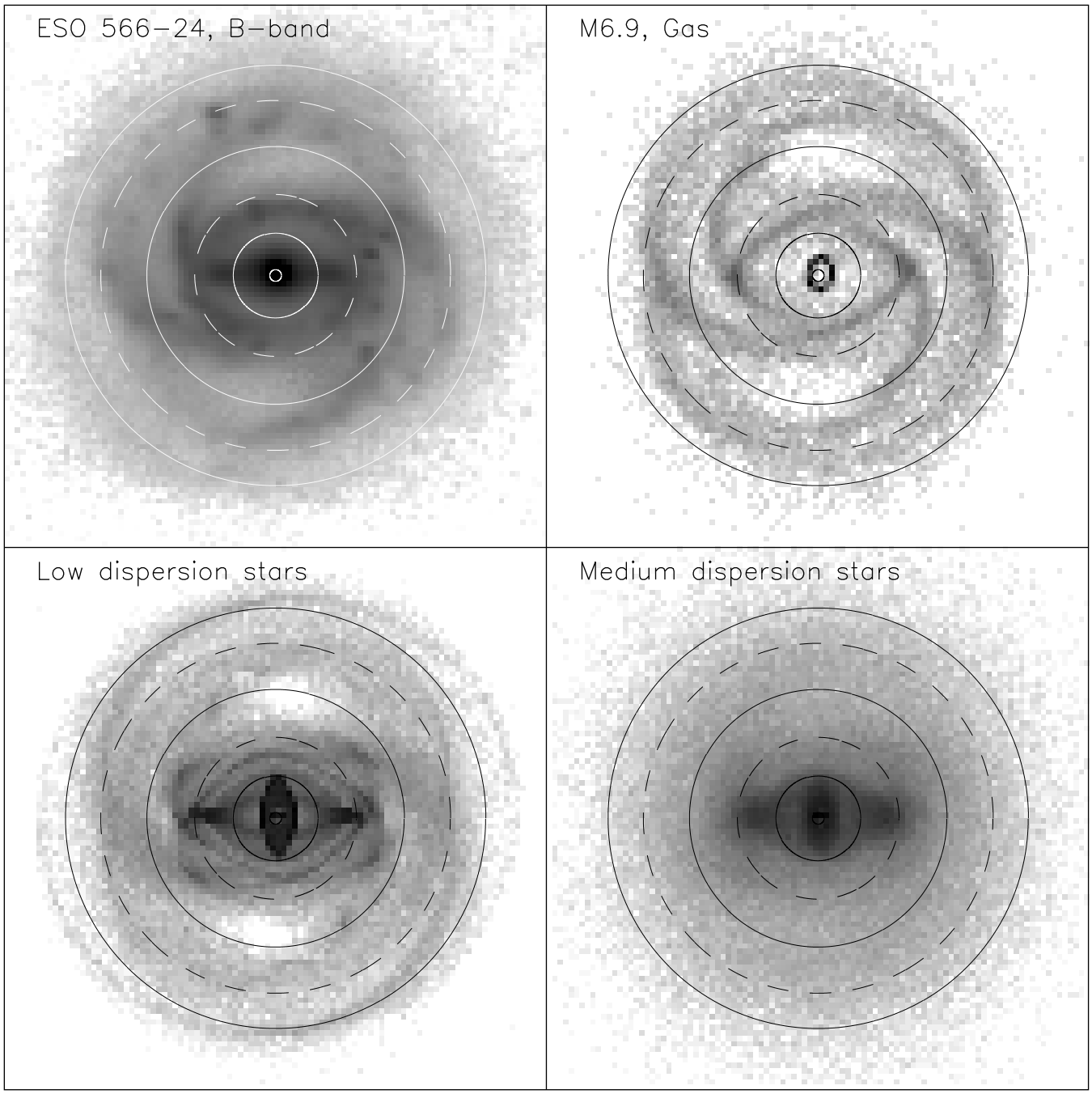


**Figure 9.** The resonance radii vs. morphology. The top left frame shows the resonance radii of model M6.9 plotted over the deprojected $B$-band image of ESO 566-24, in the top right frame they are plotted over the gas morphology of the model. The bottom frames show the morphologies of two populations of non-colliding test particles. In the low dispersion case, the velocity dispersion is about 1% of the local circular velocity, while in the medium dispersion case it is about 30% of the circular velocity. The circles drawn with a continuous line show the inner Lindblad resonance, the corotation resonance, and the outer Lindblad resonance, whereas the circles drawn with a dashed line shows the inner and outer 4/1-resonance radii. To increase resolution, the simulation images are made by summing particle positions of 10 different timesteps after the bar has reached its full strength. The width of the frames is $120''$.

disappears when this region is depopulated of gas particles. The importance of $x_2$-like orbits is further demonstrated by the kinematics of models which lack them: the plateau is replaced by a strong peak (M9.8 for example).

## 6 DISCUSSION

### 6.1 Spiral morphology in barred galaxies

The original form of the Hubble classification of galaxies (Hubble 1926) divided spiral galaxies into subclasses a, b and c, depending not only the relative size of the

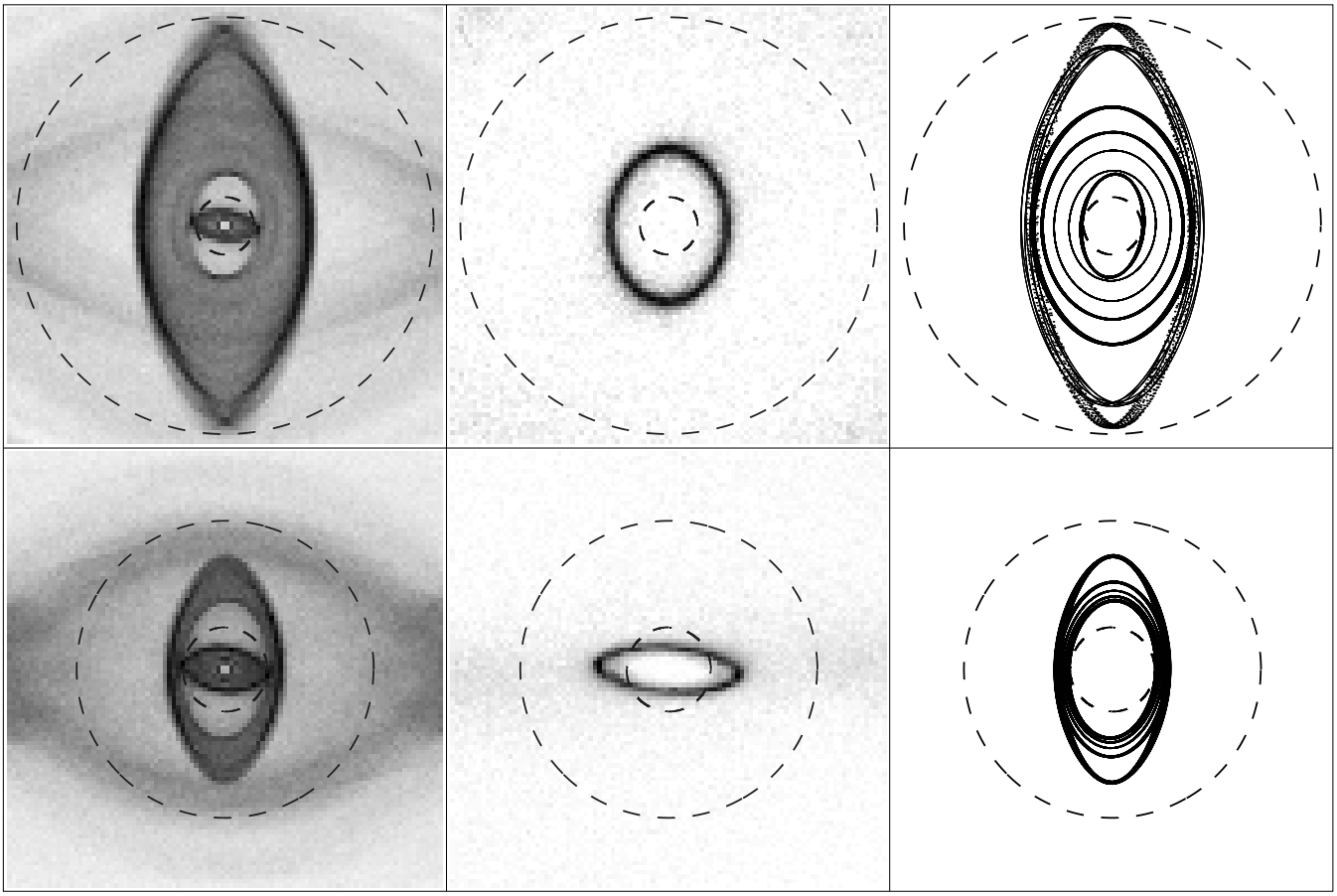

**Figure 10.** Stellar and gaseous nuclear rings vs. $x_2$-like orbits. The top row shows model M6.9, the left frame shows the low velocity stellar particles, the middle frame the gaseous nuclear ring, and the right frame selected stellar particle orbits. The bottom row shows the same for model M9.8. Outer and inner ILRs are indicated by circles drawn with a dashed line. The width of the frames is $20''$.

bulge, but also on the pitch angle of the spiral arms and the degree of resolution in the arms. Subsequent modifications or extensions (de Vaucouleurs 1959; Sandage 1961; Sandage & Bedke 1994; Buta 1995), have partially removed the limitations of the original classification, e.g. by providing description of ring and pseudoring morphologies. A different kind of spiral classification scheme was developed by Elmegreen & Elmegreen (1982, 1987). Simplifying their classification, most spiral galaxies can be divided into grand design, multiple-armed, and flocculent spiral galaxies. Grand design spirals have a global, usually two-armed spiral structure. In multiple-armed galaxies, the spiral structure starts as two-armed, but the arms bifurcate later to several outer arms. Flocculent spirals have fragmented or chaotic spiral structure.

A classic case of a barred spiral galaxy is NGC 1300, where a two-armed spiral structure starts from the ends of the bar. Quite often, the spiral arms emerge from an inner ring that surrounds the bar. There are also cases where the spiral arms start offset with respect to the ends of the bar. This can happen both in the leading and trailing quadrants of the bar (supposing that the spiral structure is trailing). Two-armed grand design structure is not the only possibility in barred galaxies. Different kinds of arm multiplicities also exist: arm bifurcation at large radius, doubled arms (one or both), and even genuine multiple-arm structure. Flocculent barred galaxies are rare but known (Buta 1995). According to Elmegreen & Elmegreen (1995), the length of the two-armed phase correlates with bar length: it reaches about twice the bar radius.

Most work on galaxy morphology has been done using $B$-band plates. A major weakness of this is that the blue wavelength region is affected by dust extinction and the young stellar population, which usually constitutes only a minor part of the mass distribution. On the other hand, in the NIR most of the light comes from the old stellar population. It has been shown that bars are more often detected in the NIR (Eskridge et al. 2000), and there are cases where the multiple-arm or flocculent spiral morphology of visual images disappears and a two-armed grand design spiral emerges in the NIR (Block & Wainscoat 1991; Block et al. 1996, 1999). It has sometimes been claimed that this kind of dualistic morphology is universal (Block & Puerari 1999). However, Eskridge et al. (2002), who used a large galaxy sample, demonstrated that dramatical differences between visual and NIR morphology are exceptions, and that in general galaxy morphology is quite similar in these two wavelength regions.

The study by Eskridge et al. (2002), based on the Ohio State University Bright Galaxy Survey (hereafter OSU-

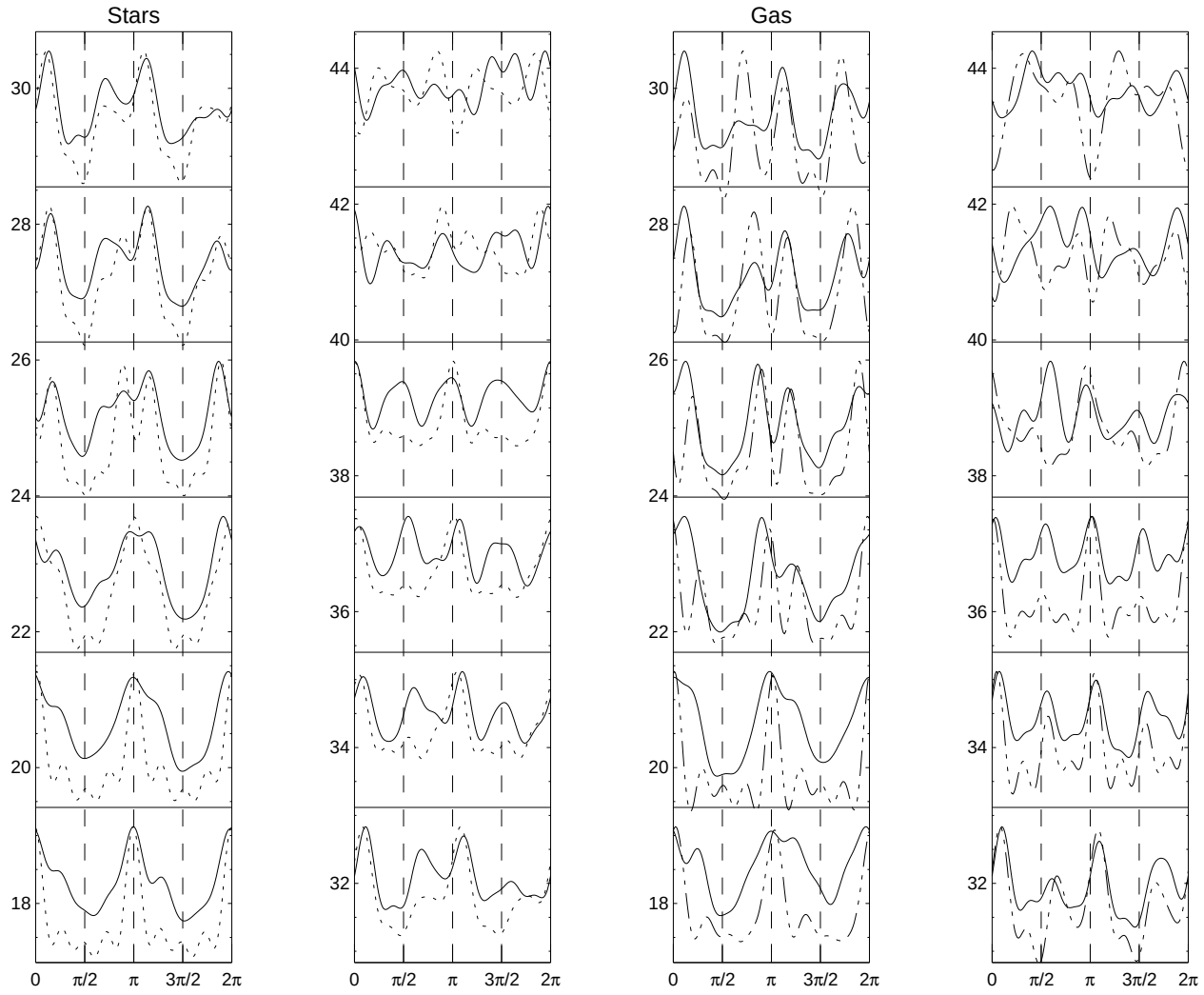


**Figure 11.** The azimuthal variations of surface density at different radii (normalized to mean density at this distance) constructed from the Fourier decomposition of images. Each curve is calculated for the radius indicated by a line below it. The phase angle of the bar is zero. The two frames on the left side compare non-colliding test particles (low dispersion case) with the $H$-band image, and the frames on the right side compare gas particles with the $B$-band image.

survey), includes several barred galaxies where the multiple-arm structure is seen also in NIR images. The examples include all variations of arm multiplicities from arm bifurcations to arm doublings and genuine multiple-armed spirals. For example, there are three-armed spiral galaxies, e.g. NGC 5054 (OSU-survey, another example is NGC 7137 Grosbøl & Patsis 1999). Although there are several four-armed galaxies in the OSU sample, none of them is similar to ESO 566-24. Most cases are arm bifurcations at large radius or doubled arms, which are close to each o her. Even in cases where the extra arms do not form as bifurcations or doublings of an $m = 2$ spiral, they are usually weaker than the dominating two arms.

ESO 566-24 with its very regular four-armed spiral structure is really exceptional. The four arms have roughly the same length, so they do not appear to have formed as a bifurcation of a usual two-armed structure. Furthermore, they are so far from each other (at $35''$, the phase difference between the arms is about $90^\circ$), that arm doubling is clearly not the case. To crown the status of ESO 566-24 as a genuine $m = 4$ spiral, the arms have comparable strength also in the NIR. Thus, one cannot choose any pair of arms, say those starting near the bar ends, as two major arms. In the OSU-survey, the galaxy with the closest resemblance to ESO 566-24 is NGC 613. It has altogether five spiral arms, but the "extra" arms are not as strong and regular as in ESO 566-24.

Some barred galaxies have features called plumes, i.e. short arcs besides the main spiral arms in the leading side with respect to the bar (Buta 1984). The best-known case is NGC 1433 (Buta 1986; Ryder et al. 1996). It is possible that plumes could be related to four-armed spiral structure, for example, they could be remnants of additional spiral arms. However, such features can form in gasdynamical simulations as result of doubled spiral arms (Byrd et al. 1994).

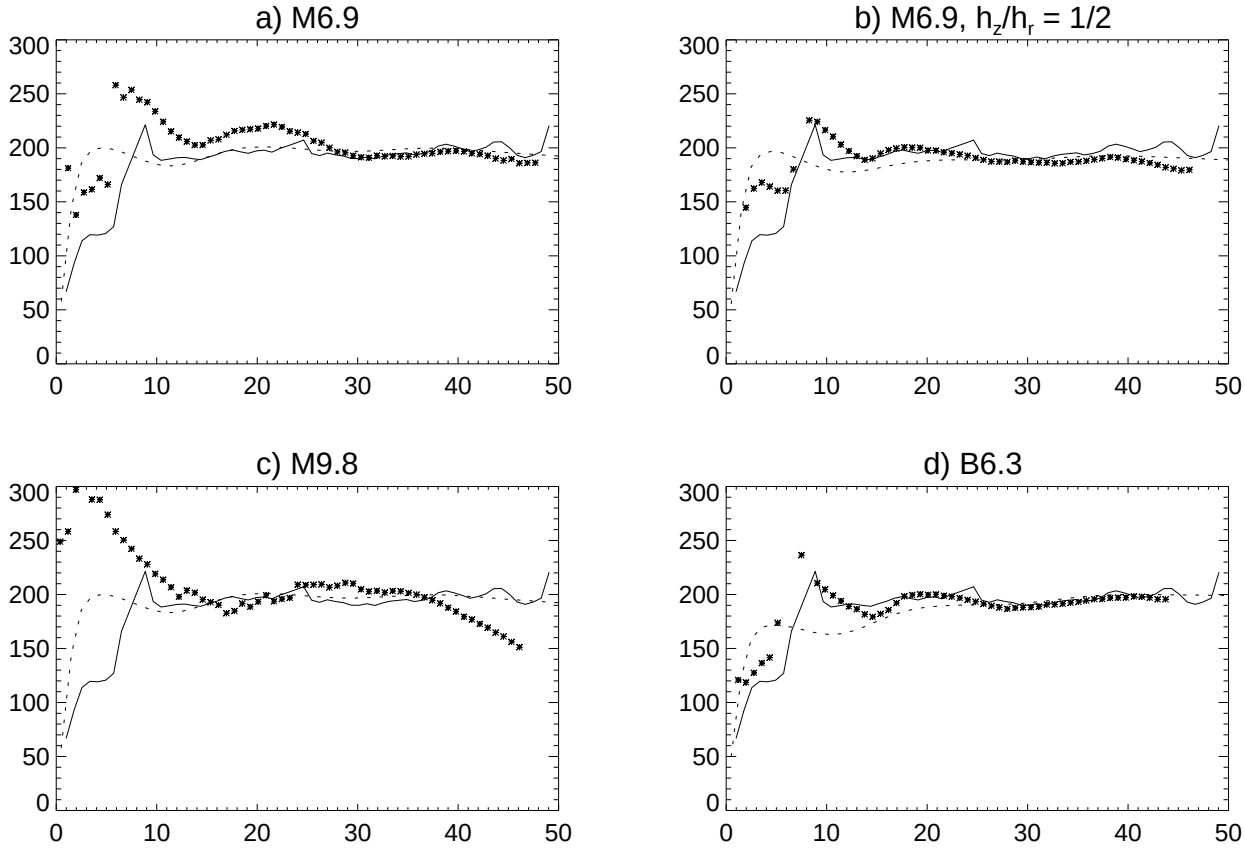


**Figure 12.** Comparison between the observed and modelled kinematics. The continuous line shows the observed "rotation curve", derived from the velocity field using the method by Warner et al. (1973). The dotted line shows the axisymmetric rotation curve based on the mass model and asterisk symbols show the simulated rotation curve constructed in the same way as the observed one.

It would be interesting to thoroughly compare ESO 566-24 with NGC 1433.

Although our best-fitting models can reproduce the four-armed spiral rather well, and give constraints to essential model parameters, they do not directly unveil the origin of such structure. Instead, even in the best case, our models are snapshots of the current stage of the evolution of ESO 566-24. It is possible that the location of resonances can give a clue of the origin of the four-armed spiral. Based on our models, it seems that four-armed structure is approximately confined between inner and outer 4/1-resonances. Thus the situation could be analogous to two-armed spirals, which are sometimes suggested to end near OLR (e.g. Elmegreen et al. 1989). Note however, that at least for non-barred galaxies, other solutions, which put the end of the spiral structure inside corotation or even the inner 4/1-resonance, have also been suggested (Patsis et al. 1994, 1997).

### 6.2 Rings

A connection between rings and resonances was perhaps first suggested by Schommer & Sullivan (1976), who identified two rings in NGC 4736 with inner and outer Lindblad resonances. Later, sticky particle simulations by Schwarz (1981, 1984b,a) showed that gas can accumulate near the resonance radii. These and other studies (Combes & Gerin 1985; Byrd et al. 1994; Rautiainen & Salo 2000) have identified nuclear rings with orbits near the ILR, inner rings near the inner 4/1-resonance and outer rings near the OLR. Two different observed populations of outer rings and pseudorings (Buta 1995) are nicely explained by orbits inside and outside OLR: inside OLR the major axes of the orbits belonging to the dominating orbit family are oriented perpendicular to the bar, whereas outside OLR they are oriented parallel to the bar.

In many studies, the nuclear rings in single bar potentials have been identified with $x_2$-orbits, which are perpendicular to the bar. When the non-axisymmetric perturbation is weak, and the deviations from circular motion are small, the outermost stable $x_2$-orbits reach the ILR (or the outer ILR when there are two inner Lindblad resonances) (Contopoulos & Grosbøl 1989). However, when the strength of the perturbation is increased, the linear approximation is not valid, and the outermost extent of $x_2$-orbits moves inwards. In fact, some authors have redefined the ILR-radius so that it means the radius with the outermost stable $x_2$-orbits (van Albada & Sanders 1982; Athanassoula 1992a; Miwa & Noguchi 1998).

Recently, Regan & Teuben (2003) have studied the formation and evolution of nuclear rings using a hydrodynam-

ics code with an analytic bar potential. Their conclusion is that the nuclear rings are not related to inner Lindblad resonances, but instead they form as an interaction between gas streaming along $x_2$- and $x_1$-like streamlines. Furthermore, the nuclear rings in their simulations did not have a steady size but shrank throughout the simulation. Such behaviour can be seen also in our simulations, but the change in the size of the nuclear ring becomes very slow in the later phases of the simulations. This can be due to lack of interaction with particles on $x_1$-like orbits, which have become depopulated.

We have tested the hypothesis by Regan and Teuben that the nuclear rings form as interaction of two different gas streamlines by making simulations where all the particles initially resided in the domain of $x_2$-like orbits. A clear nuclear ring formed without interaction of two streamlines. In fact, a nuclear ring may form even without any gas: the redistribution of non-colliding test particles by a rotating bar also forms a "concentration" of particles near the outermost $x_2$-like orbits. Rings can form also in self-gravitating stellar particles of N-body simulations (Rautiainen & Salo 2000; Athanassoula & Misiriotis 2002). In ESO 566-24, the inner ring is clearly present in the $H$-band, and corresponding examples exist also for outer and nuclear rings. Byrd et al. (1994) speculated that stellar rings could be remnants of star formation in gaseous rings, but it is also possible that a ring forms as a response of the old stellar population to a non-axisymmetric potential.

If the rings are connected to orbits in the presence of a non-axisymmetric bar potential, then the shapes of the rings should correlate with the bar strength. Buta (2002) compared the shapes of the inner rings in a few galaxies with the $Q_b$-parameter, and did not find a clear correlation. Galaxies with roughly similar $Q_b$ values can have inner rings of different shapes, ranging from virtually circular to highly elongated. This can be explained in several ways. First, $Q_b$ measures the peak strength of the bar, which often takes place well inside the inner ring, i.e. $Q_b$ may not be representative of tangential force in the ring region. This effect can be seen in action in Figs. 5 – 7: in the higher pattern speed models, the inner ring is located closer to centre, in a region with higher $Q_T$, which explains the more elongated shape ($Q_b$ is constant in each pattern speed series). Second, the $Q_b$ values were calculated from NIR photometry, and thus the possible contribution of dark matter was omitted.

### 6.3 Pattern speed dilemma

Our best-fitting models have pattern speeds which place the corotation resonance at about 1.6 times the bar radius. This is considerably larger than the often cited value $r_{CR}/r_{bar} = 1.2\pm0.2$. For IC 4214 we found a value of $1.4\pm0.2$ (Salo et al. 1999), thus just barely fitting within the fast bar regime although it has an early-type morphology. This raises a question if our modelling method is biased so that it gives too high values. Our preliminary results with NGC 4314 suggest otherwise; for this galaxy we get $r_{CR}/r_{bar}$ close to one.

We extended a previous study by Elmegreen (1996) by a brief search of the literature. We found pattern speed determinations of individual barred galaxies giving values ranging from below 1 to over 2, the average value being about 1.35 (median value was 1.3). The values based on the Tremaine-Weinberg method tend to be close to 1, although Aguerri et al. (2003) found considerably higher values for galaxies NGC 1440 ($1.6^{+0.5}_{-0.3}$) and NGC 3412 ($1.5^{+0.6}_{-0.3}$). Furthermore, the Tremaine-Weinberg method has been used almost exclusively with SB0-galaxies. ESO 566-24 is of Hubble type SB(r)b, later than most galaxies whose pattern speed has been determined with the Tremaine-Weinberg method. Elmegreen & Elmegreen (1985) have suggested that early-type galaxies have longer bars than late-type galaxies in both the physical size and with respect to resonance locations. Thus, it seems possible that the high value found in our study could somehow be related to Hubble type.

A point in favour of higher pattern speeds is the existence of dust lanes inside the bar. According to Athanassoula (1992b) the offset dust lanes form when the galaxy has an ILR and their shape corresponds to the observations when the corotation radius is $1.2\pm0.2$ times the bar radius. However, the dust lane argument for fast bars may not be as strong as it seems: Lindblad & Kristen (1996) found two possible pattern speeds for NGC 1300, giving $r_{CR}/r_{bar} = 1.3$ and $r_{CR}/r_{bar} = 2.4$, both producing good dust lane morphology.

N-body studies have shown that pattern speeds of the bar and spiral arms can be different, structures being either separate or in a non-linear mode coupling (Sellwood & Sparke 1988; Masset & Tagger 1997; Rautiainen & Salo 1999). Rautiainen & Salo (2000) demonstrated that rings can form also in self-gravitating simulations with two or more modes with different pattern speeds. Sometimes, the presence of two strong modes caused cyclic evolution in the shape and orientation of the ring. At least in the case of nuclear rings, this can be attributed to orbit loops (Maciejewski & Sparke 2000) in a potential with two rotating components (Rautiainen et al. 2002). So, in principle it is it possible that ESO 566-24 could be modelled with two modes: the inner region having a higher pattern speed and the four-armed spiral a pattern speed in the range of our single pattern models. However, in this case the low value for the pattern speed is based not only on the modelling of the four-armed spiral structure, but also the central morphology is better modelled with low pattern speed: the inner and nuclear rings have approximately the right size. When the pattern speed is higher, both become too elongated or disappear altogether.

### 6.4 Halo contribution

Early N-body simulations of barred galaxies (Sellwood 1981) exhibited deceleration of the bar rotation due to interaction with the outer disk. This made the corotation radius to move outwards, but it was compensated by the growth of the bar, i.e. the bar always ended close to corotation. However, interaction between bar and dark halo can introduce bar slowdown that cannot be compensated by bar growth. Weinberg (1985) studied the dynamical friction between a bar and halo analytically and also by a "semi-resticted" N-body simulation (particles are not self-gravitating), and found that it causes the bar to lose most of its angular momentum in just a few bar rotations. Little & Carlberg (1991) studied bar slowdown by self-gravitating N-body models, where both the disk and halo were two-dimensional. The bar deceleration in their model was considerably lower, only by a factor of two

during 10 Gyr, half of which was due to interaction with the outer disk. On the other hand, Hernquist & Weinberg (1992) who used an analytical bar with a self-gravitating halo, found a slowdown rate corresponding to that found by Weinberg.

At least seemingly confusing results have been obtained also with fully self-consistent N-body models of bar–halo interaction. Debattista & Sellwood (1998, 2000) find that in models with centrally concentrated haloes, the bar slows down dramatically ($r_{CR}/r_{bar} > 1.4$), unless the halo has unrealistically high angular momentum in the same direction as the disk. Valenzuela & Klypin (2002) made simulations using adaptive grid refinement (the potential grid was subdivided in high density regions), which increased the gravity resolution. They found that the bar pattern speed was almost constant and that the stellar disk lost only 5 – 10% of its angular momentum to the halo. Furthermore, they could reproduce the dramatic bar slowdown when the grid resolution was decreased. Recently, Athanassoula (2003) found that when the halo velocity dispersion is increased, the bar slowdown rate also decreases.

The preceding discussion indicates that it is questionable whether bar pattern speed can be used as an argument for high or low halo-to-disk mass ratios. If we compare our best-fitting mass model with the simulations of Debattista & Sellwood (1998) with a non-rotating halo, and adopt their parameter $\eta = (v_{disk}/v_{halo})^2$ at the maximum of disk rotation curve, we find $\eta = 3.65$. In their Fig. 2, this would correspond to $r_{CR}/r_{bar} = 1.3 - 1.4$ at the final equilibrium state. On the other hand, if we include bulge to $v_{halo}$, we get $\eta = 1.39$, corresponding $r_{CR}/r_{bar} > 2$ in Debattista & Sellwood (1998). Debattista & Sellwood (2000) found that a halo which rotates in the same sense as the bar can induce lower bar slowdown rate than non-rotating or retrograde halos. When taking into account that bulges rotate, our result $r_{CR}/r_{bar} \approx 1.6$ is not in disagreement with results of Debattista & Sellwood (1998, 2000). However, the situation is the same if we compare with simulations by Valenzuela & Klypin (2002): in their models the corotation resonance radius is 1.2 to 1.7 times the bar radius, and our value is near the upper limit of their range.

In our best fitting model (M6.9), the dark halo contributes less than 20% of the mass inside $r_{2.2}$. The rotation curve is dominated by luminous matter even inside the whole disk region. Thus, our results with ESO 566-24 are in accordance with estimates of disk mass contribution by dynamical modelling (e.g. Weiner et al. 2001), but disagree with cold dark matter (CDM) cosmological N-body simulations, which produce cuspy halos (e.g. Navarro et al. 1996)

## 7 CONCLUSIONS

We have constructed dynamical models for the four-armed barred spiral galaxy ESO 566-24. The mass distribution of the different components is based on near-IR photometry with the exception of a possible dark halo, whose amount was chosen to fit the rotation curve at large radii. We have been able to construct a model which reproduces the observed four-armed morphology. Also the main kinematic characteristics are seen in our models. The main conclusions are as follows.

1. Two major factors affecting the simulated morphology and kinematics are the strength of the non-axisymmetric perturbation and the pattern speed of the bar. The former depends on the mass and the thickness of the disk.

2. Both the kinematical and morphological fits are better when a moderate halo component is included. On the other hand, a dominating halo can be ruled out, because then the gas response to the disk gravitational potential is too weak. Thus, the contribution of the luminous matter dominates the rotation curve in the whole optical disk.

3. The four-armed spiral could be produced between the inner and outer 4/1-resonances. The inner ring is close to the inner 4/1-resonance and the nuclear ring is between two inner Lindblad resonances. The size of the nuclear ring seems to correlate with the size of the region suitable for non-crossing $x_2$-like orbits.

4. If the bar has the same pattern speed as the four-armed spiral, then it rotates rather slowly; the corotation radius is about $1.6 \pm 0.3$ times the bar radius (including uncertainties both in the bar radius and pattern speed), which is higher than the often cited value of $1.2 \pm 0.2$. The existence of several other determined high values for this ratio suggests that there is more scatter in the $r_{CR}/r_{bar}$ ratio than is sometimes stated. It should also be noted that most bar pattern speed determinations have been made for galaxies of earlier Hubble type than ESO 566-24.

5. The rather high value of $r_{CR}/r_{bar}$ is difficult to be disputed by pattern speed multiplicity. In addition to the spiral structure, the nuclear and inner rings can be reproduced in the right scale with a single pattern speed. Adopting considerably higher pattern speeds, which would be consistent with the bar ending near corotation, produce significantly worse-fitting ring morphology. Also, the kinematics of the central parts deviate more from the observed velocities.

6. The relatively slow bar rotation rate can be due to interaction between the bar and the spheroidal component (halo and bulge). The exceptional $m = 4$ spiral morphology can be related to the low bar rotation rate and the importance of the spheroidal component.

7. The curious shape of the inner rotation curve can be explained by combined effects of $x_1$- and $x_2$-like orbits.

## ACKNOWLEDGMENTS

This work has been supported by Väisälä Foundation and by the Academy of Finland. RB acknowledges the support of NSF grant AST-0205143 to the University of Alabama. This work made use of data from the Ohio State University Bright Spiral Galaxy Survey, which was funded by grants AST-9217716 and AST-9617006 from the United States National Science Foundation, with additional support from the Ohio State University.

## REFERENCES

Aguerri J. A. L., Debattista V. P., Corsini E. M., 2003, MNRAS, 338, 465
Athanassoula E., 1992a, MNRAS, 259, 328
Athanassoula E., 1992b, MNRAS, 259, 345
Athanassoula E., 2002, ApJL, 569, L83

Athanassoula E., 2003, MNRAS, 341, 1179
Athanassoula E., Misiriotis A., 2002, MNRAS, 330, 35
Ball R., 1992, ApJ, 395, 418
Binney J., Tremaine S., 1987, Galactic dynamics. Princeton, NJ, Princeton University Press, 1987
Block D. L., Elmegreen B. G., Wainscoat R. J., 1996, Nature, 381, 674
Block D. L., Puerari I. ., 1999, A&A, 342, 627
Block D. L., Puerari I. ., Frogel J. A., Eskridge P. B., Stockton A., Fuchs B., 1999, AP&SS, 269, 5
Block D. L., Wainscoat R. J., 1991, Nature, 353, 48
Buta R., 1984, PASAu, 5, 472
Buta R., 1986, ApJS, 61, 631
Buta R., 1988, ApJS, 66, 233
Buta R., 1995, ApJS, 96, 39
Buta R., 2002, ASP Conf. Ser. 275: Disks of Galaxies: Kinematics, Dynamics and Peturbations, p. 185
Buta R., Alpert A. J., Cobb M. L., Crocker D. A., Purcell G. B., 1998, AJ, 116, 1142
Buta R., Block D. L., 2001, ApJ, 550, 243
Buta R., Combes F., 1996, Fundamentals of Cosmic Physics, 17, 95
Buta R., Combes F., 2000, ASP Conf. Ser. 197: Dynamics of Galaxies: from the Early Universe to the Present, p. 11
Buta R., Crocker D. A., 1991, AJ, 102, 1715
Buta R., Crocker D. A., 1993, AJ, 105, 1344
Buta R., Purcell G. B., 1998, AJ, 115, 484
Buta R., Purcell G. B., Cobb M. L., Crocker D. A., Rautiainen P., Salo H., 1999, AJ, 117, 778
Buta R., Ryder S. D., Madsen G. J., Wesson K., Crocker D. A., Combes F., 2001, AJ, 121, 225
Byrd G., Rautiainen P., Salo H., Buta R., Crocher D. A., 1994, AJ, 108, 476
Canzian B., 1993, ApJ, 414, 487
Canzian B., Allen R. J., 1997, ApJ, 479, 723
Combes F., Elmegreen B. G., 1993, A&A, 271, 391
Combes F., Gerin M., 1985, A&A, 150, 327
Combes F., Sanders R. H., 1981, A&A, 96, 164
Contopoulos G., Grosbøl P., 1989, A&AR, 1, 261
de Grijs R., 1998, MNRAS, 299, 595
de Grijs R., Peletier R. F., van der Kruit P. C., 1997, A&A, 327, 966
de Vaucouleurs G., 1959, Handbuch der Physik, 53, 275
Debattista V. P., Sellwood J. A., 1998, ApJ, 493, L5
Debattista V. P., Sellwood J. A., 2000, ApJ, 543, 704
Duval M. F., Athanassoula E., 1983, A&A, 121, 297
Elmegreen B., 1996, ASP Conf. Ser. 91: IAU Colloq. 157: Barred Galaxies, p. 197
Elmegreen B. G., Elmegreen D. M., 1985, ApJ, 288, 438
Elmegreen B. G., Seiden P. E., Elmegreen D. M., 1989, ApJ, 343, 602
Elmegreen D. M., Elmegreen B. G., 1982, MNRAS, 201, 1021
Elmegreen D. M., Elmegreen B. G., 1987, ApJ, 314, 3
Elmegreen D. M., Elmegreen B. G., 1995, ApJ, 445, 591
England M. N., 1989, ApJ, 344, 669
Eskridge P. B., Frogel J. A., Pogge R. W., Quillen A. C., Berlind A. A., Davies R. L., DePoy D. L., Gilbert K. M., Houdashelt M. L., Kuchinski L. E., Ramírez S. V., Sellgren K., Stutz A., Terndrup D. M., Tiede G. P., 2002, ApJS, 143, 73
Eskridge P. B., Frogel J. A., Pogge R. W., Quillen A. C., Davies R. L., DePoy D. L., Houdashelt M. L., Kuchinski L. E., Ramírez S. V., Sellgren K., Terndrup D. M., Tiede G. P., 2000, AJ, 119, 536
Grosbøl P. J., Patsis P. A., 1999, ASP Conf. Ser. 182: Galaxy Dynamics - A Rutgers Symposium, p. 217
Hernquist L., Weinberg M. D., 1992, ApJ, 400, 80
Hubble E. P., 1926, ApJ, 64, 321
Kent S. M., 1986, AJ, 91, 1301
Kent S. M., 1987, AJ, 93, 1062
Knapen J. H., Shlosman I., Peletier R. F., 2000, ApJ, 529, 93
Kranz T., Slyz A., Rix H., 2001, ApJ, 562, 164
Laurikainen E., Salo H., 2002, MNRAS, 337, 1118
Laurikainen E., Salo H., Rautiainen P., 2002, MNRAS, 331, 880
Lindblad P. A. B., Kristen H., 1996, A&A, 313, 733
Lindblad P. A. B., Lindblad P. O., Athanassoula E., 1996, A&A, 313, 65
Little B., Carlberg R. G., 1991, MNRAS, 250, 161
Maciejewski W., Sparke L. S., 2000, MNRAS, 313, 745
Maoz D., Barth A. J., Sternberg A., Filippenko A. V., Ho L. C., Macchetto F. D., Rix H. ., Schneider D. P., 1996, AJ, 111, 2248
Masset F., Tagger M., 1997, A&A, 322, 442
Merrifield M. R., Kuijken K., 1995, MNRAS, 274, 933
Miwa T., Noguchi M., 1998, ApJ, 499, 149
Navarro J. F., Frenk C. S., White S. D. M., 1996, ApJ, 462, 563
Ostriker J. P., Peebles P. J. E., 1973, ApJ, 186, 467
Patsis P. A., Grosbøl P., Hiotelis N., 1997, A&A, 323, 762
Patsis P. A., Hiotelis N., Contopoulos G., Grosbøl P., 1994, A&A, 286, 46
Rautiainen P., Salo H., 1999, A&A, 348, 737
Rautiainen P., Salo H., 2000, A&A, 362, 465
Rautiainen P., Salo H., Laurikainen E., 2002, MNRAS, 337, 1233
Regan M. W., Teuben P., 2003, ApJ, 582, 723
Rix H., Rieke M. J., 1993, ApJ, 418, 123
Ryder S. D., Buta R. J., Toledo H., Shukla H., Staveley-Smith L., Walsh W., 1996, ApJ, 460, 665
Sackett P. D., 1997, ApJ, 483, 103
Salo H., Rautiainen P., Buta R., Purcell G. B., Cobb M. L., Crocker D. A., Laurikainen E., 1999, AJ, 117, 792
Sandage A., 1961, The Hubble atlas of galaxies. Washington: Carnegie Institution, 1961
Sandage A., Bedke J., 1994, The Carnegie atlas of galaxies. Washington, DC: Carnegie Institution of Washington with The Flintridge Foundation
Schommer R. A., Sullivan W. T., 1976, Astrophysical Letters, 17, 191
Schwarz M. P., 1981, ApJ, 247, 77
Schwarz M. P., 1984a, MNRAS, 209, 93
Schwarz M. P., 1984b, A&A, 133, 222
Sellwood J. A., 1981, A&A, 99, 362
Sellwood J. A., Sparke L. S., 1988, MNRAS, 231, 25P
Sempere M. J., Garcia-Burillo S., Combes F., Knapen J. H., 1995, A&A, 296, 45
Teuben P. J., 2002, ASP Conf. Ser. 275: Disks of Galaxies: Kinematics, Dynamics and Perturbations, p. 217
Tremaine S., Weinberg M. D., 1984, ApJ, 282, L5
Valenzuela O., Klypin A., 2002, astro-ph/0204028

van Albada T. S., Sanders R. H., 1982, MNRAS, 201, 303
Warner P. J., Wright M. C. H., Baldwin J. E., 1973, MNRAS, 163, 163
Weinberg M. D., 1985, MNRAS, 213, 451
Weiner B. J., Sellwood J. A., Williams T. B., 2001, ApJ, 546, 931